Ore Geology Reviews 165 (2024) 105866

Contents lists available at ScienceDirect

Ore Geology Reviews

journal homepage: www.elsevier.com/locate/oregeorev

A rare sellaite-bearing orogenic gold deposit at Pianyanzi, Yangtze Craton: Ore genesis as implied from *in-situ* studies of pyrite

Qiu-Ming Pei [a,*], Cheng-Hong Li [a], Shao-Bing Ma [a], Yi Liang [a], Hua-Wen Cao [b], Hang-Fei Ge [a], Jia-Le Shen [a], Inna Safonova [a,c,*]

[a] Faculty of Geosciences and Environmental Engineering, Southwest Jiaotong University, Chengdu 611756, China
[b] State Key Laboratory of Oil and Gas Reservoir Geology and Exploitation, Chengdu University of Technology, Chengdu 610059, China
[c] Sobolev Institute of Geology and Mineralogy SB RAS, Koptyuga ave. 3, Novosibirsk 630090, Russia

ARTICLE INFO

Keywords:
Sellaite
Pyrite
In-situ analyses
Orogenic gold deposit
Ore genesis
Pianyanzi

ABSTRACT

The Pianyanzi gold deposit is situated at the western margin of the Yangtze Craton, and represents a rare sellaite-bearing orogenic gold deposit. This deposit belongs to the Dauduhe gold belt of southwestern China and remains poorly documented. In this paper we present first petrographic and *in-situ* geochemistrical and sulfur isotope data from pyrite as well as results of multielement mapping. The deposit is dominated by native gold (average gold fineness = 980.8) filling fractures in minerals (e.g., pyrite, quartz, sellaite and hematite) or also emplaced along the contact interface between mineral grains. Pyrite is the most abundant sulfide mineral of this deposit. We identified five generations of pyrite: Py1, Py2a, Py2b, Py3, and Py4. Gold occurs in sellaite- and hematite-bearing mineral assemblages formed simultaneous with the formation of Py2a&b and Py4, respectively. Py1 formed in the Au-poor ore stage, while Py3 formed during the late galena-dominated sulfide stage. All generations of pyrite exhibit low concentrations of gold with an average value of less than 2 ppm. Py2a&b possess distinctive textures and chemical zonation, with trace elements displaying greater variations compared to Py1, Py3 and Py4. The $\delta^{34}S$ values vary from −0.52 ‰ to 7.08 ‰, which is consistent with those of orogenic deposits of the Daduhe gold belt. The deep metasomatized mantle lithosphere acted as a potential source of ore fluids. We conclude that the co-precipitation of native gold and sellaite was triggered by the interaction between auriferous fluids and dolomite.

1. Introduction

Orogenic gold deposits, also known as epigenetic lode- to disseminated-style gold-only deposits in metamorphic rocks, generally form at convergent margins during *syn*-subduction accretion to late-subduction lithosphere thinning or even continental collision (Gebre-Mariam et al., 1995; Groves et al., 1998; Robert et al., 2007; Goldfarb et al., 2019; Wang et al., 2022; Safonova and Perfilova, 2023; Zeng et al., 2023). Gold deposits of this type are widely distributed throughout the world and account for a significant proportion of the world's gold resources and production (Goldfarb et al., 2005; Weatherley and Henley, 2013; Chinnasamy et al., 2015). Numerous studies have demonstrated that the formation of orogenic gold deposits coincides well with the amalgamation of supercontinents (Barley and Groves, 1992; Goldfarb et al., 2001; Bierlein et al., 2009; Groves and Santosh, 2021; Wang et al., 2023), indicating that studying such deposits can contribute to reconstructing the tectonic evolution of individual accretionary and/or collisional orogens and supercontinents. Consequently, the orogenic gold deposits have recently attracted significant attention of researchers worldwide (Phillips and Powell, 2009; Huston et al., 2012; Deng and Wang, 2016; Groves et al., 2020; Zhao et al., 2021; Zhao et al., 2022b; Goldfarb and Pitcairn, 2023; Vasilopoulos et al., 2023; Raič et al., 2023).

Orogenic gold deposits represent one of the most important types of gold deposits in China and typically occur along the margins of cratons and adjacent orogenic belts (Wang et al., 2022 and references therein). The Daduhe gold belt (also known as the Daduhe–Jinpingshan gold belt) is extended along the western margin of the Yangtze Craton. It is a famous gold metallogenic belt in southwest China with more than thirty gold deposits discovered (Wang et al., 2005; Li et al., 2007; Deng and Wang, 2016; Wang et al., 2020; Zhao et al., 2022a). Despite the common

* Corresponding authors at: Faculty of Geosciences and Environmental Engineering, Southwest Jiaotong University, Chengdu 611756, China (Q.-M. Pei and I. Safonova).
E-mail addresses: pqm@swjtu.edu.cn (Q.-M. Pei), inna03-64@mail.ru (I. Safonova).

https://doi.org/10.1016/j.oregeorev.2023.105866
Received 3 December 2023; Received in revised form 25 December 2023; Accepted 31 December 2023
Available online 4 January 2024

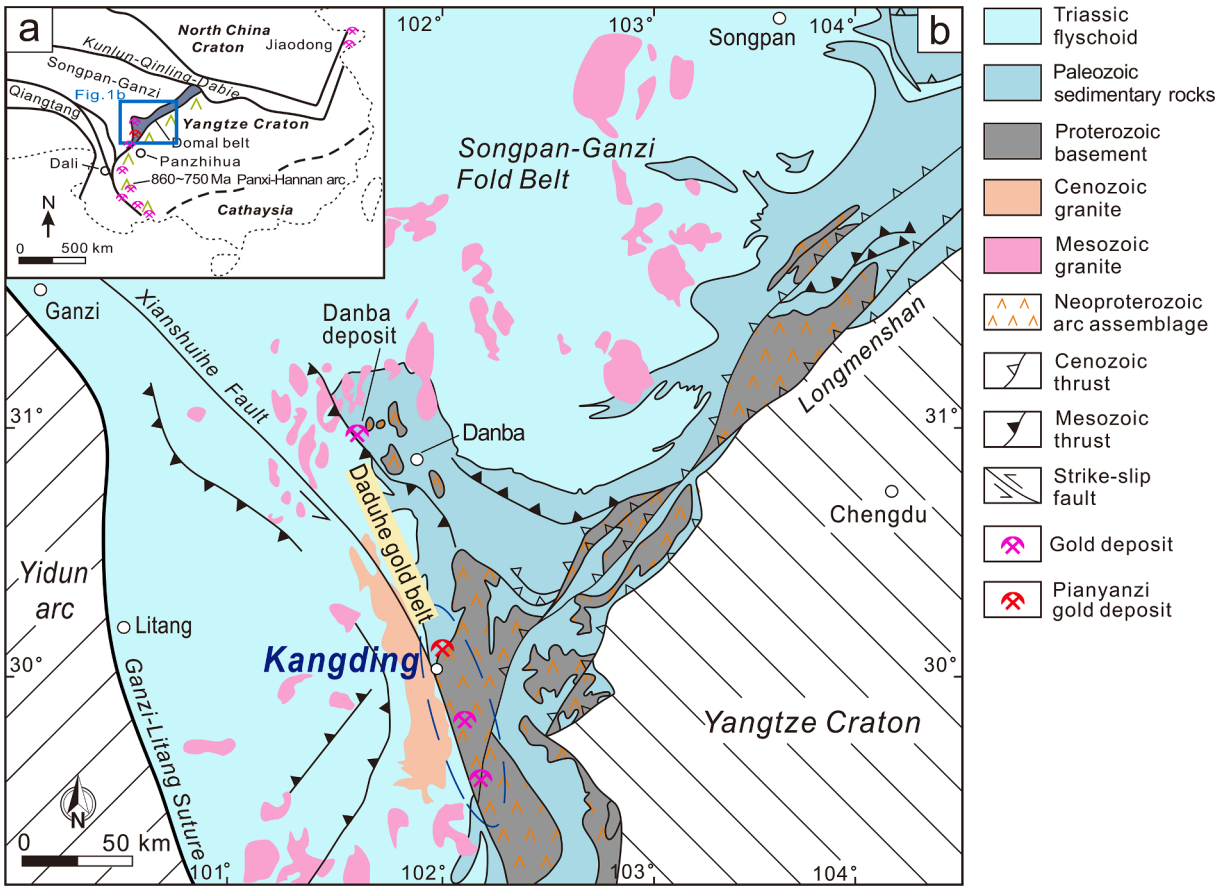

Fig. 1. (a) Simplified tectonic map showing the location of the western margin of the Yangtze Craton (modified after Wang et al. 2020). (b) Regional geological map showing the stratigraphy, magmatic rocks, structures, and gold deposits (modified after Zhao et al. 2022b).

features of orogenic gold systems, some aspects such as fluid/metal sources and mineral assemblages also show great differences (e.g., Large et al., 2011; Goldfarb and Groves, 2015; Qiu et al., 2020; Yang et al., 2023). The Pianyanzi deposit is located in the middle Daduhe gold belt and carry specific sellaite-bearing mineral assemblages (sellaite–quartz–sulfide–fluorite–quartz–Au), which are untypical of orogenic gold deposits. Previous studies have revealed that diverse mineral assemblages in orogenic gold systems can be caused by diverse ore fluids, structural settings and host rocks through specific geological processes such as fluid-rock interaction (Hodkiewicz et al., 2009; Williams-Jones et al., 2009; Groves et al., 2018; Yang et al., 2021). However, the specifics of such processes in this deposit remain unclear. Early studies focused mostly on geologic features, ore-controlling structures and fluid inclusions (Mao et al., 1986; Luo et al., 1987; Lu and Mao, 1988; Li and Cai, 1995; Zheng, 1995; Zhang et al., 2022), but recently there have appeared new tools and methods like *in-situ* high-resolution mineral-scale analysis. In this paper we present first results from "traditional" and in-situ studies of pyrite of the Pianyanzi deposit.

Pyrite is a ubiquitous sulfide in hydrothermal systems, which can form in a wide range of fluid temperatures, oxygen fugacities and pH conditions (Craig et al., 1998; Fontboté et al., 2017). The texture and chemical composition of pyrite keep a record of physicochemical conditions of the fluid from which it crystallized (Cook et al., 2009; Koglin et al., 2010; Gregory et al., 2016; Gregory et al., 2019). In addition, the sulfur isotope geochemistry of pyrite is crucial to interpret the sources and evolution of ore-forming fluids during successive hydrothermal and metamorphic events (e.g., Tanner et al., 2016; Hu et al., 2019; Sun et al., 2020; Cao et al., 2021; Martin et al., 2023). Accordingly, pyrite is ideally suitable for high-precision *in-situ* measurements coupled with trace element and sulfur isotope analyses to decipher complex and poorly constrained gold mineralization processes (Tanner et al., 2016; Keith et al., 2020; Ma et al., 2022; Berthier et al., 2023; Chao et al., 2023; Yang et al., 2023). Here, we report new field and petrographic observations, *in-situ* geochemistry and sulfur isotopic compositions of pyrite of the poorly studied Pianyanzi gold deposit. In attempting to better examine trace element variations, *in-situ* multielement mapping was also conducted in this contribution. Additionally, we analyzed the concentrations of Au and Ag in native gold grains formed in different paragenetic stages. The main goals of the present work were to elucidate: (1) the nature of sellaite-bearing gold mineralization; (2) the multielement and sulfur isotopic variations in different pyrite generations; and (3) the occurrence and precipitation mechanisms of Au.

2. Geological background

2.1. Regional geology

The Pianyanzi gold deposit is situated in the western margin of the Yangtze Craton, China (Fig. 1a). The structural framework of this region has been established during a multistage tectonic evolution: 1) the Neoproterozoic oceanic spreading and subduction (Zhou et al., 2002; Zhao and Zhou, 2008; Zou et al., 2021); 2) Late Paleozoic continental rift and mantle plume (Xu et al., 2007; Deng et al., 2014; Li et al., 2016; Metcalfe, 2021); 3) Mesozoic Paleo-Tethys suturing (Yan et al., 2011; Zhang et al., 2023); and 4) Cenozoic uplift of the eastern Tibetan Plateau related to the India–Asia collision (Cao et al., 2017; Kapp and DeCelles, 2019; Su et al., 2019; Cao et al., 2023a). Stratigraphically, along the large-scale Mesozoic domal belt of the northwestern Yangtze Craton (Fig. 1a), the exposed Mesoproterozoic to Neoproterozoic crystalline basement essentially consists of Neoproterozoic arc

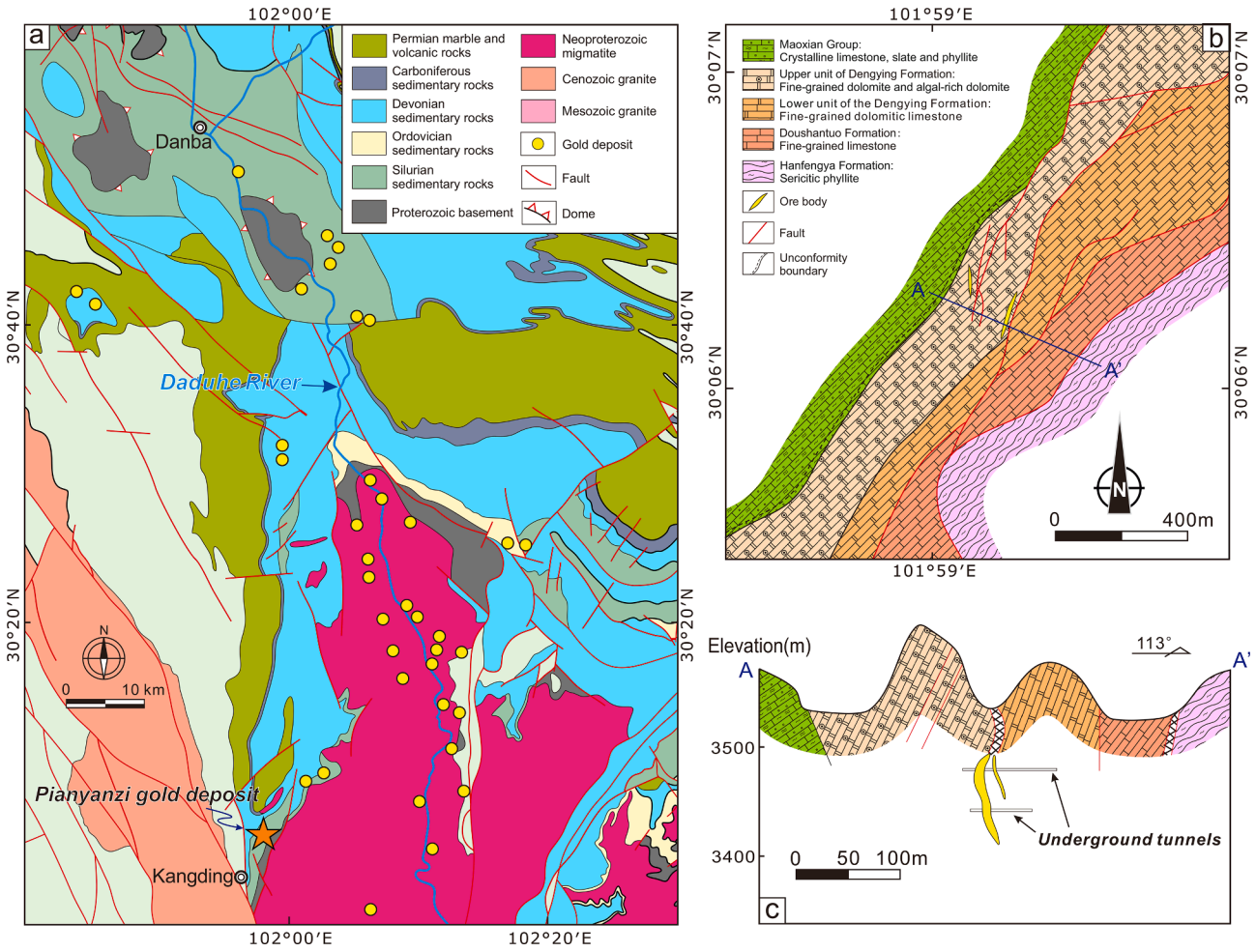

Fig. 2. (a) Geological map of the Duduhe gold belt (modified after Zhao et al. 2022a). (b) Geological sketch map of the Pianyanzi gold deposit (modified after Luo et al. 1987). (c) Simplified geological profile of the Pianyanzi gold deposit (modified after Luo et al. 1987).

plutonic–metamorphic assemblages (Wallis et al., 2003; Zhou et al., 2006). The basement complexes (e.g., the Kangding complex) include granitic gneisses, gneiss granites and migmatites and are largely overlain by a Neoproterozoic (Sinian) to Cenozoic cover sequence (Zhou et al., 2006; Yan et al., 2018), which is dominated by Paleozoic strata and Triassic flysch (Fig. 1b). The India–Asia collision resulted in the compression, which generated a system of ductile–brittle shear zones and faults of variable scales and rates (Yan et al., 2018). Such a network of tectonic structures appeared to be favorable for the formation of diverse hypogene deposits (Groves and Santosh, 2021; Yang et al., 2022; Zhou et al., 2023), in particular, significant amounts of gold deposits have been identified on the both sides of the Daduhe River to form the Daduhe gold belt. Abundant igneous rocks are distributed in this region and are mainly composed of Proterozoic mafic–ultramafic rocks, layered Permian mafic rocks related to the Emeishan large igneous province (LIP), and Mesozoic and Cenozoic granitoids (Zhang et al., 2009; Roger et al., 2010; Cao et al., 2022; Zhao et al., 2022a), all could provide necessary material, power and heat sources for mineralization (Broom-Fendley et al., 2017; Pei et al., 2017; Pei et al., 2022).

2.2. Ore deposit geology

The Pianyanzi deposit (>5 t Au @ 2.5 g/t) is located 6 km north of Kangding City in western Sichuan Province, Southwest China (Fig. 2a). It has a long history of sporadic mining dating back ~ 100 years, but the amount of Au ores extracted during the early period is unknown, and therefore the size of the deposit has been underestimated (Luo et al., 1987). The later investigations of minerals and fluid inclusions provided more knowledge about the ore genesis (e.g., Mao et al., 1986; Lu and Mao, 1988; Li and Cai, 1995, Zheng, 1995; Zhang et al., 2022).

The numerous gold deposits/occurrences distributed in the Kangding area and around all form the Kangding gold district (Fig. 2a). As shown in Fig. 2b, the exposed strata of the Pianyanzi deposit mainly consist, from oldest to youngest, of the Ediacaran Doushantuo and Dengying Formations, the Silurian Maoxian Group, and the upper Triassic Hanfengya Formation. The Doushantuo Formation is exposed in the southeastern part of the mining area and is mainly composed of fine-grained limestone. The Dengying Formation can be divided into two units: (1) the lower unit of fine-grained dolomitic limestone; and (2) the upper unit of fine-grained dolomite and algal-rich dolomite. The upper unit of the Dengying Formation hosts the gold ore bodies (Fig. 2b). The Maoxian Group comprises crystalline limestone, slate and phyllite, which are exposed in the western part of the deposit. The Hanfengya Formation crops out in the southeast corner of the deposit and consists of sericitic phyllite interbedded with sandy slate. The structural framework of the deposit consists of earlier N–S-striking faults and later fanning NW- to NE-striking faults and matches that of the whole Daduhe gold belt (Wang et al., 2020; Zhao et al., 2022a). The gold ore bodies are mainly hosted in the NNE–NE-trending extensional faults and fractures. The majority of the ore bodies are buried and can be explored only by underground mining or drilling (Fig. 2c). The ore bodies are steadily extending by the strike and/or the ore veins show no tendency to pinch out.

The dominant metallic minerals at Pianyanzi are pyrite, hematite,

Stages / Minerals	Ore forming stages				Post-ore stage
	Stage 1	Stage 2	Stage 3	Stage 4	
Ore minerals in vein					
Pyrite	Py1	Py2a Py2b	Py3	Py4	
Native gold					
Galena					
Sphalerite					
Chalcopyrite					
Hematite					
Limonite					
Chalcocite					
Enargite					
Scheelite					
Alteration and gangue					
Quartz					
Sellaite					
Fluorite					
Dolomite					
Calcite					
Malachite					
Azurite					
Sulfur					

Major Common Minor Trace

Fig. 3. Mineral paragenesis and assemblage diagram of the Pianyanzi gold deposit.

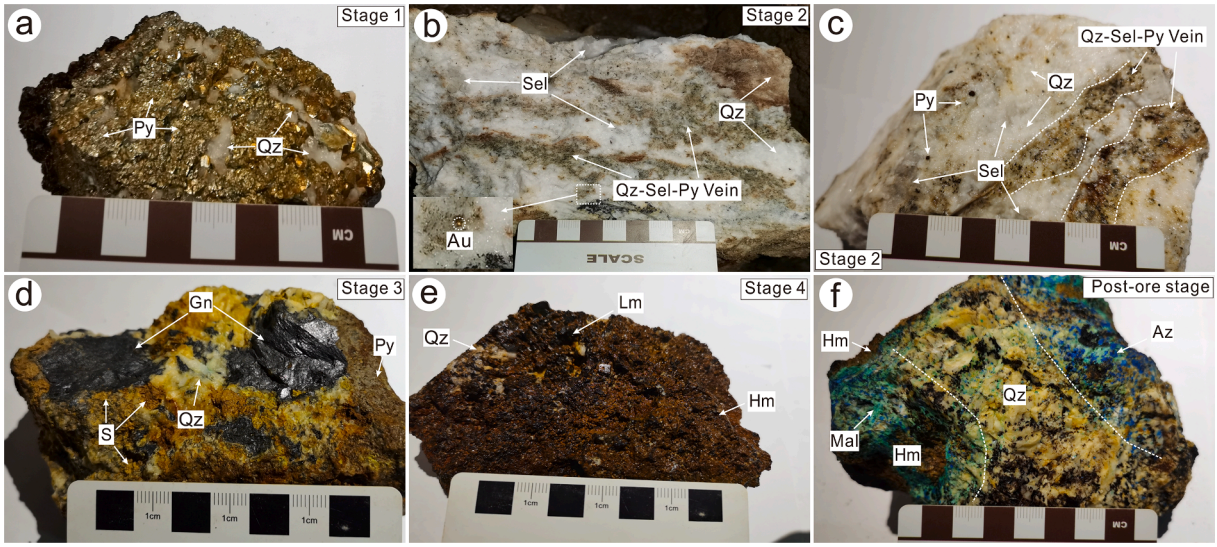

Fig. 4. Photographs of hand specimens showing the mineralization and mineral assemblages of the Pianyanzi gold deposit. a. Coarse-grained pyrite in barren quartz veins in stage 1; b–c. Sellaite-bearing gold ore in stage 2; d. Galena, pyrite, native sulfur within quartz in stage 3; e. hematite-bearing gold ore in stage 4; f. Malachite + azurite + hematite + quartz in post-ore stage (stage 5). Abbreviations: Gn–galena, Hm–hematite, Lm–limonite, Mal–malachite, Py–pyrite, Qz–quartz, Sel–sellaite.

galena, native gold, chalcopyrite, sphalerite, limonite and chalcocite. Gangue minerals mainly include sellaite, fluorite, quartz, malachite and carbonates. We identified four ore-forming stages and one post-ore stage on the basis of cross-cutting relationships, textures of hand-size and microscopic specimen and observed mineral assemblages (Fig. 3). Stage 1: crystallization of milky barren quartz and coarse-grained euhedral–subhedral pyrite (Fig. 4a). Stage 2: crystallization of sellaite and formation of economic amounts of native gold (Fig. 4b) plus abundant euhedral pyrite, quartz with minor galena, fluorite, dolomite, and subordinate sphalerite, enargite, scheelite and calcite (Fig. 4c). Stage 3: deposition of later sulfides, abundant galena, pyrite and quartz with minor sphalerite (Fig. 4d). Stage 4: crystallization of grey–white quartz with abundant coarse-grained anhedral–subhedral hematite, deposition of economic amounts of native gold, plus pyrite and limonite (Fig. 4e). Stage 5 is post-ore epigenetic oxidation that formed widespread oxidized minerals such as malachite and limonite (Fig. 4f).

As mentioned above, the economic gold mineralization of the Pianyanzi deposit developed in Stage 2 and Stage 4. A special feature of Stage 2 mineral assemblage is the presence of sellaite. Sellaite is a transparent mineral that typically occurs as coarse anhedral grains with

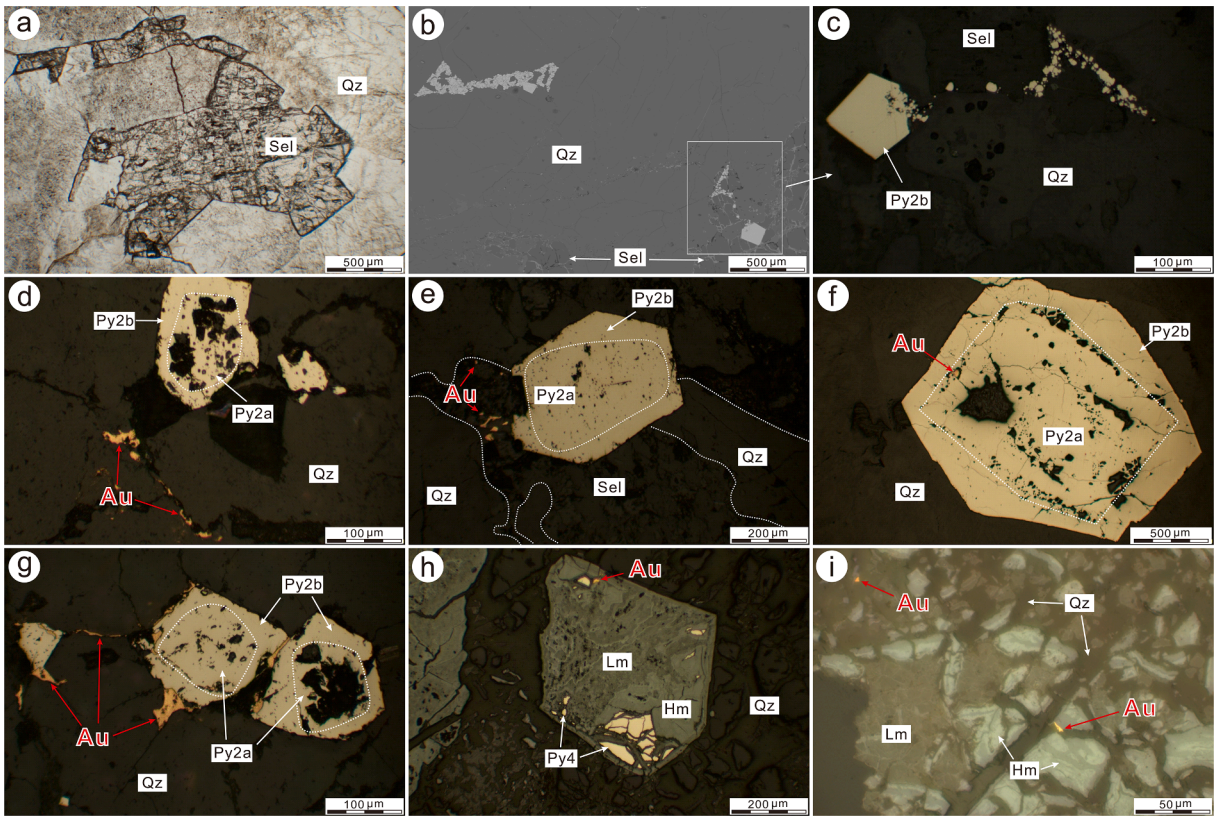

Fig. 5. Photomicrographs illustrating ore textures and gold occurrence of the Pianyanzi gold deposit. a. Transmitted light image showing sellaite and quartz. B. BSE image of pyrite, sellaite and quartz. c. Reflected light (RL) image of crushed pyrite grains intergrown with sellaite and quartz. RL images showing native gold occurring as discrete grains within quartz (d), sellaite (e) and pyrite (f), or along grain boundaries (g). h–i. RL images showing native gold grains in hematite of stage 4. Abbreviations: Hm–hematite, Py–pyrite, Qz–quartz, Sel–sellaite.

high negative relief under microscope (Fig. 5a). It is very closely associated with quartz, fluorite, pyrite and native gold (Fig. 5b–c). The Stage 2 gold mineralization is characterized by discrete gold grains (2–100 μm) occurring within other mineral grains (Fig. 5d–f) or along grain boundaries (Fig. 5g). Stage 4 is marked by large amounts of oxidized minerals (e.g., hematite) (Fig. 5h). Hematite is the most abundant mineral and can sometimes form through the replacement of pre-existing pyrite (Fig. 6). Compared to Stage 2, Stage 4 has a similar occurrence of gold, but produces less gold and smaller native gold grains (less than 20 μm).

The weak proximal hydrothermal alteration is aligned linearly and is manifested in silicification, pyritization, sericitization, chloritization and carbonatization of the zone around the ore veins and ore-controlling faults.

3. Sampling and analytical techniques

Twenty-five samples of different types of ores and wall rocks were collected from field outcrops and two underground tunnels within the mining area at the 3412 and 3300 m altitude levels for this study. Polished thin sections were made from both barren samples and gold-bearing ores of different mineralization stages at Guangzhou Tuoyan Analytical Technology Co. Ltd. (Guangzhou, China). Detailed petrographic and mineralogical examinations were studied via reflected and transmitted polarized light microscopy and electron microprobe analysis (EMPA). Subsequently, a total of eleven pyrite-bearing samples with typical mineral assemblages were further selected for in-situ elemental content and sulfur isotope analyses.

The EMPA was undertaken using a JEOL JXA–8230 electron probe at the School of Geoscience and Technology, Southwest Petroleum University, China. The thin sections were uniformly carbon-coated (20 nm thick) prior to analysis. All analyses for sulfide were carried out under the following conditions: accelerating voltage = 20 kV, beam current = 20nA, beam diameter = 1 μm, and counting time for each element = 10 s. The measured elements are Se, S, Bi, Fe, Cu, Zn, As, Co, Ni, Sb, Ag, Pb and Au. All data were corrected using a standard ZAF routine, yielding a precision of better than 1 %. Additionally, backscattered electron (BSE) images were captured during the EMPA analysis.

In-situ trace element analyses of pyrite were performed by the Laser Ablation Inductively Coupled Plasma Mass Spectra (LA–ICP–MS) at the Wuhan Sample Solution Analytical Technology Co., Ltd., Wuhan, China (WSSAT), using a GeoLasPro laser ablation system consisting of a COMPexPro 102 ArF 193 nm excimer laser and a MicroLas optical system connected to an Agilent 7700e ICP–MS instrument. The laser ablation system was equipped with a signal-smoothing device to improve the stability of the signal and precision of the isotope ratio (Hu et al., 2015). Helium was applied as the carrier gas for laser ablation and was merged with argon (makeup gas) during single-hole ablation (Cao et al., 2023b). The beam diameter was set to 15 μm for all samples and reference materials, with a pulse frequency of 5 Hz. Trace element concentrations of sulfides were calibrated against various reference materials (NIST 610 and NIST 612) without using an internal standard (Liu et al., 2008). The sulfide reference material of MASS–1 (USGS) is used as the unknown sample to verify the accuracy of the calibration method. Each analysis included a background acquisition of approximately 20–30 s followed by 50 s sample data acquisition. The analyzed elements include Li, Be, Na, Mg, Al, Si, P, S, K, Ca, Ti, Cr, Mn, Fe, S, Co, Ni, Cu, Zn, Ge, As, Se, Mo, Ag, Sb, Au, Pb and Bi. The Excel-based software ICPMSDataCal is used for offline processing of the analytical data (Liu et al., 2008).

LA–ICP–MS trace element mapping on pyrite domains was completed under a procedure similar to that for the spots except for

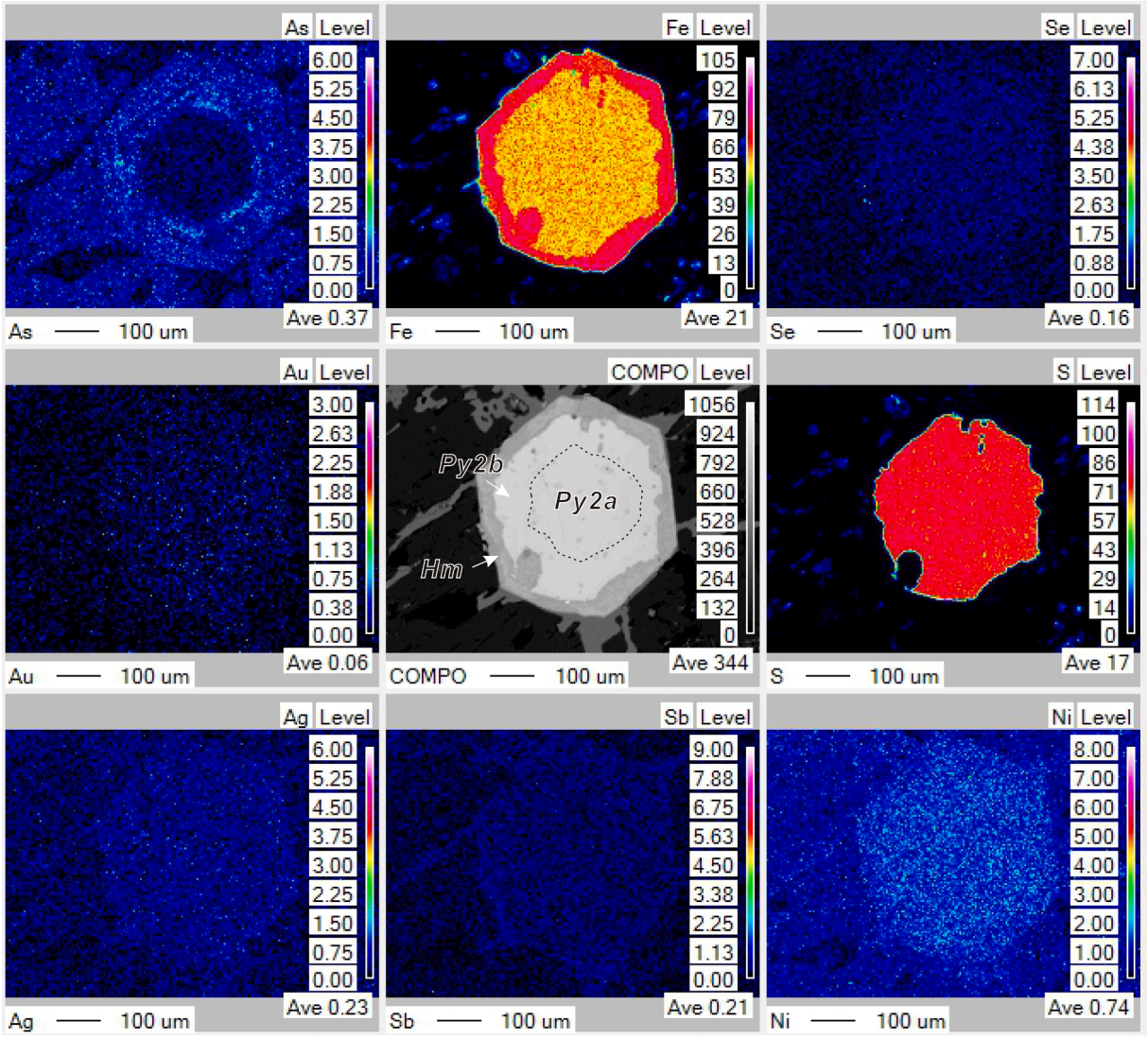

Fig. 6. EMPA element maps of selected pyrite grains from the Pianyanzi gold deposit.

slight variations in spot size and pulse rate. Instead of individual spot locations, a series of parallel lines were ablated. Accordingly, the concentration at each time slice was stacked to form an x–y concentration grid, which is displayed as false color images using a kriging algorithm (Wu et al., 2018). Detailed information about the LA–ICP–MS mapping method in pyrite is similar to that previously reported in Koenig et al. (2009).

Polished thin sections for *in-situ* trace element spot analyses of pyrite were chosen for *in-situ* sulfur isotopic analyses, which were also conducted using LA–ICP–MS method at WSSAT. Analyses were performed on a Neptune Plus MC–ICP–MS (Thermo Fisher Scientific, Bremen, Germany) together with a Geolas HD excimer ArF laser ablation system (Coherent, Göttingen, Germany). Analytical techniques are described in detail by Fu et al. (2016). Single spot ablation mode was used at a large spot size (44 μm) and low pulse frequency (2 Hz), which were used to avoid the down hole fractionation effect. During the experiment, the laser energy fluency was kept constant at ~5 J/cm^2. A standard-sample bracketing method (SSB) was employed to compensate for instrumental mass fractionation. The in-house references of pyrrhotite SP-Po-01 ($\delta^{34}S_{v\text{-}CDT}$ = 1.4 ± 0.4), chalcopyrite SP-CP-01 ($\delta^{34}S_{v\text{-}CDT}$ = 5.45 ± 0.3) and two synthetic Ag_2S standards IAEA-S-2 ($\delta^{34}S_{v\text{-}CDT}$ = 22.58 ± 0.39) and IAEA-S-3 ($\delta^{34}S_{v\text{-}CDT}$ = –32.18 ± 0.45) were analyzed repeatedly as unknown samples to ensure the accuracy of the calibration method. In addition, all data reduction for the MC–ICP–MS analysis of sulfur isotope ratios was processed with the "Iso-Compass" software (Zhang et al., 2020).

4. Results

4.1. Pyrite generations

Pyrite is the predominant sulfide mineral in this deposit. Based on petrographic observations and BSE imaging, at least five pyrite generations (Py1, Py2a, Py2b, Py3 and Py4) with distinct textures and mineral assemblages are identified throughout the mineralization stages.

The pyrite formed in the first stage of paragenesis (Py1) is mostly coarse- to medium-grained euhedral–subhedral grains (100 μm to 2 mm). Py1, mainly formed in the Au-poor ore stage, is typically inclusion free with a uniform internal texture (Fig. 7a). Late-stage dendritic hematite overgrows from the grain boundaries of Py1 displaying a replacement texture (Fig. 7b). These Py1 grains usually have irregular textures, which are interpreted to be the products of corrosion.

Py2 is commonly developed in the Au-rich main ore stage and has angular to rounded edges with crystals ranging in diameter from 30 to 500 μm. It is porous and associated with abundant sellaite, fluorite, dolomite, trace sulfide and widely distributed gold, which typically

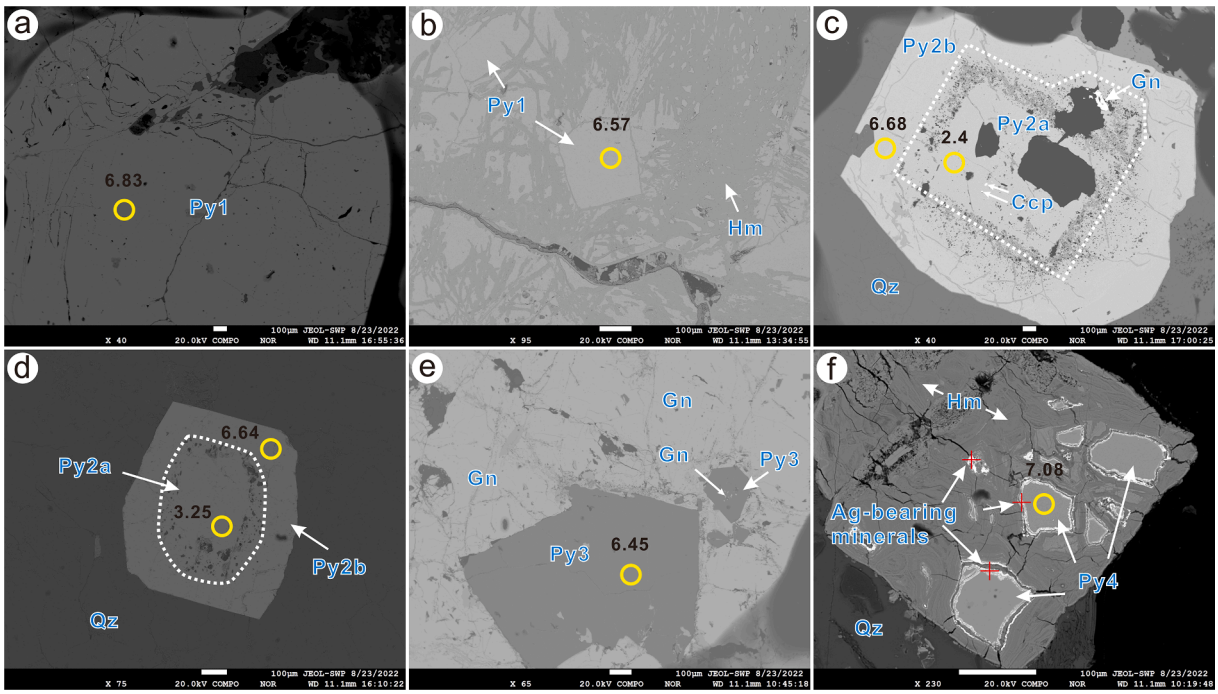

Fig. 7. BSE images with sulfur isotope sites showing representative textures of pyrites from Pianyanzi. (a) Coarse-grained euhedral–subhedral Py1 grains. (b) Hematite and pyrite form dendritic textures. (c–d) Zoned pyrite (Py2a&b) with porous structure and rich in inclusions. (e) Py3 in galena-dominant mineral assemblage. (f) Pyrite in hematite and associated Ag-bearing substances. Abbreviations: Ccp–chalcopyrite, Gn–galena, Hm–hematite, Py–pyrite, Qz–quartz.

Table 1
Summary of EMPA analyses of each pyrite generation from Pianyanzi.

types	Items	S	Fe	Cu	Zn	As	Co	Ni	Sb	Bi	Ag	Au	Total
Py1	Min	51.90	45.56	bdl	bdl	0.01	0.03	bdl	bdl	bdl	bdl	bdl	98.18
(n = 12)	Max	53.49	46.85	0.02	0.04	0.59	0.07	0.03	0.04	0.12	0.02	0.07	100.57
	Average	52.63	46.10	0.01	0.01	0.29	0.05	0.01	0.01	0.05	bdl	0.02	99.24
Py2a	Min	52.14	45.93	bdl	bdl	bdl	0.04	bdl	bdl	bdl	bdl	bdl	98.52
(n = 19)	Max	53.51	47.33	0.04	0.05	0.38	0.09	0.06	0.02	0.13	0.02	0.10	100.88
	Average	52.85	46.45	0.01	0.02	0.04	0.06	0.01	bdl	0.03	0.01	0.02	99.49
Py2b	Min	51.40	45.79	bdl	bdl	bdl	0.03	bdl	bdl	bdl	bdl	bdl	98.19
(n = 32)	Max	53.45	47.44	0.03	0.04	0.91	0.09	0.05	0.04	0.11	0.03	0.11	100.86
	Average	52.79	46.43	0.01	0.01	0.31	0.06	bdl	0.01	0.03	0.01	0.03	99.67
Py3	Min	52.09	45.71	bdl	bdl	0.10	0.04	bdl	bdl	bdl	bdl	bdl	98.61
(n = 5)	Max	53.09	46.26	0.02	0.03	0.96	0.06	0.01	bdl	0.02	0.03	bdl	99.53
	Average	52.71	46.08	0.01	0.01	0.34	0.05	bdl	bdl	0.01	0.02	bdl	99.22
Py4	Min	52.41	45.81	bdl	bdl	0.01	0.03	bdl	bdl	bdl	bdl	bdl	98.75
(n = 10)	Max	53.53	46.69	0.05	0.02	0.39	0.08	0.02	0.02	0.12	0.06	0.10	100.30
	Average	53.01	46.23	0.02	bdl	0.15	0.06	bdl	0.01	0.04	0.02	0.02	99.54

Note: bdl = below detection limit.

occur as particles within or along the microfractures of Py2 (Fig. 7c). The core–rim textures were best developed in this generation of pyrite and thus Py2 can be further subdivided into Py2a and Py2b. Their overgrowth relationship and general succession can be easily identified by BSE images (Fig. 7c–d), indicating that they contain higher concentrations of other elements such as As. Py2b commonly borders Py2a as thin subhedral rims. In particular, the zoned or oscillatory-rimmed pyrite commonly consists of cavities, an inclusion-rich core (Py2a) and an inclusion-poor rim (Py2b).

Py3 typically coexists with galena, sphalerite, and quartz in Stage 3. It appears as euhedral crystals varying from 100 to 500 μm (Fig. 7e). Py4 is found in irregular shapes surrounded by hematite, often appearing as discrete grains with a size of less than 50 μm (Fig. 7f). Native gold grains are also sparsely present in the fractures within hematite adjacent to Py4 (Fig. 5h). In addition, both Py3 and Py4 are texturally homogeneous and have very few inclusions.

4.2. EMPA analysis of pyrite and native gold

The major element compositions of different pyrite generations were determined through a total of 78 EPMA spot analyses. The results are summarized in Table 1, and the full data sets are available in supplementary Table 1. No significant compositional variations were detected by EMPA. The Fe, S and Co contents among all pyrite types have restricted ranges of 45.6–47.4 %, 51.4–53.5 % and 0.03–0.09 %, respectively. In terms of arsenic, slight variations were observed among the different types of pyrite. Specifically, the average As contents in Py1, Py2a, Py2b, Py3 and Py4 are 0.29 %, 0.04 %, 0.31 %, 0.34 % and 0.15 %, respectively. EMPA mapping in selected pyrite grains also yields similar element variation trends (Fig. 6). In addition, elements such as Se, Bi, Cu, Zn, Ni, Sb, Ag, Pb and Au were sometimes below the detection limit of EMPA.

The Au and Ag concentrations of native gold grains in different ore stages were also measured with EMPA. All analytical data are provided

Table 2
Summary of LA–ICP–MS spot analyses of each pyrite generation from Pianyanzi.

Pyrites types	Items	Co	Ni	Cu	Zn	As	Se	Ag	Sb	Au	Pb	Bi	Mg	Ca
Py1	Min	0.02	0.02	0.34	0.92	2197.16	bdl	bdl	0.02	0.14	0.03	0.01	0.01	bdl
(n = 9)	Max	2.08	10.07	7.49	38.15	4724.39	58.94	0.30	30.97	1.90	49.08	2.44	23.00	55.09
	Average	0.28	1.77	2.32	5.57	3348.21	24.56	0.06	3.94	0.68	6.05	0.34	5.57	18.67
Py2a	Min	0.07	0.18	1.78	1.12	0.19	4.23	0.01	0.02	0.01	0.02	0.01	0.04	3.02
(n = 16)	Max	48.97	41.60	591.43	102.64	969.67	151.59	10.41	35.27	3.47	1059.86	29.09	13518.91	23741.55
	Average	8.64	9.18	45.22	8.18	185.82	48.74	1.87	9.09	0.75	118.57	3.76	1154.69	2400.69
Py2b	Min	0.01	0.12	0.24	1.12	616.68	2.49	0.02	0.04	0.27	0.08	0.01	0.04	0.73
(n = 24)	Max	86.23	350.37	11.84	19.44	10656.39	181.98	7.88	41.99	12.48	1381.18	11.69	537.92	711.15
	Average	20.66	44.59	3.87	2.43	4460.23	41.05	1.24	3.66	2.99	127.84	1.23	46.85	70.40
Py3	Min	0.02	0.16	1.05	0.90	1166.55	2.28	0.05	0.04	0.41	0.31	bdl	0.24	10.12
(n = 5)	Max	2.79	16.39	3.24	1.62	2912.98	87.84	2.60	36.41	2.61	218.61	bdl	0.46	38.40
	Average	0.90	4.24	1.91	1.30	1929.48	31.73	0.73	12.68	1.08	98.49	bdl	0.37	21.66
Py4	Min	0.20	0.05	0.24	0.84	717.43	14.59	0.16	0.02	0.07	0.95	0.01	0.11	7.38
(n = 5)	Max	1.95	1.27	5.46	2.22	1224.25	90.44	127.45	0.21	2.00	13.22	0.22	0.19	38.47
	Average	1.15	0.69	1.92	1.41	967.71	51.25	43.38	0.07	0.71	5.69	0.12	0.14	22.61

Note: bdl = below detection limit.

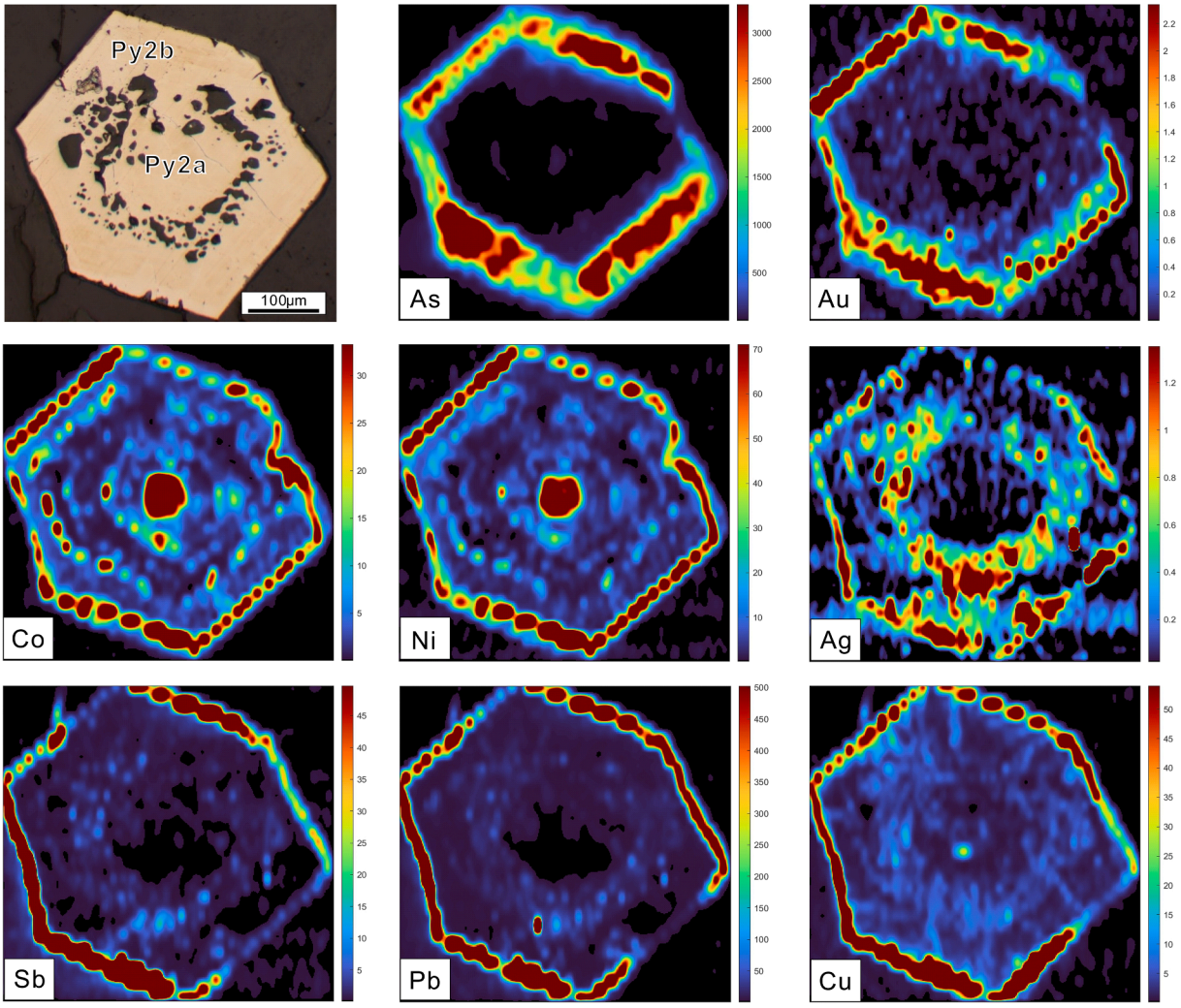

Fig. 8. LA–ICP–MS multielement mapping of selected pyrite from the Pianyanzi gold deposit.

in supplementary Table 2. The 55 spot analyses of Stage 2 and Stage 4 are similar to each other, with gold fineness (=Au (wt %)/[Au (wt %) + Ag (wt %)] × 1000) ranging from 976.4 to 986.9 and 960.9 to 992.9, respectively. The mean values of gold fineness in Stage 2 and Stage 4 are 981.4 (N = 27) and 980.3 (N = 28), respectively. The above results show that the native gold grains in the Pianyanzi gold deposit exhibit constant and high Au contents.

4.3. LA–ICP–MS trace element analysis of pyrite

Trace element data for all generations of pyrite obtained by LA-ICP-MS spot analysis are summarized in Table 2 and Fig. 10. The complete data sets are compiled in Supplementary Table 3. Some representative profiles of various pyrites are presented in Fig. 11. All generations of pyrite in the Pianyanzi deposit have various As, Pb, Co, Ni, Au, Ag, Cu,

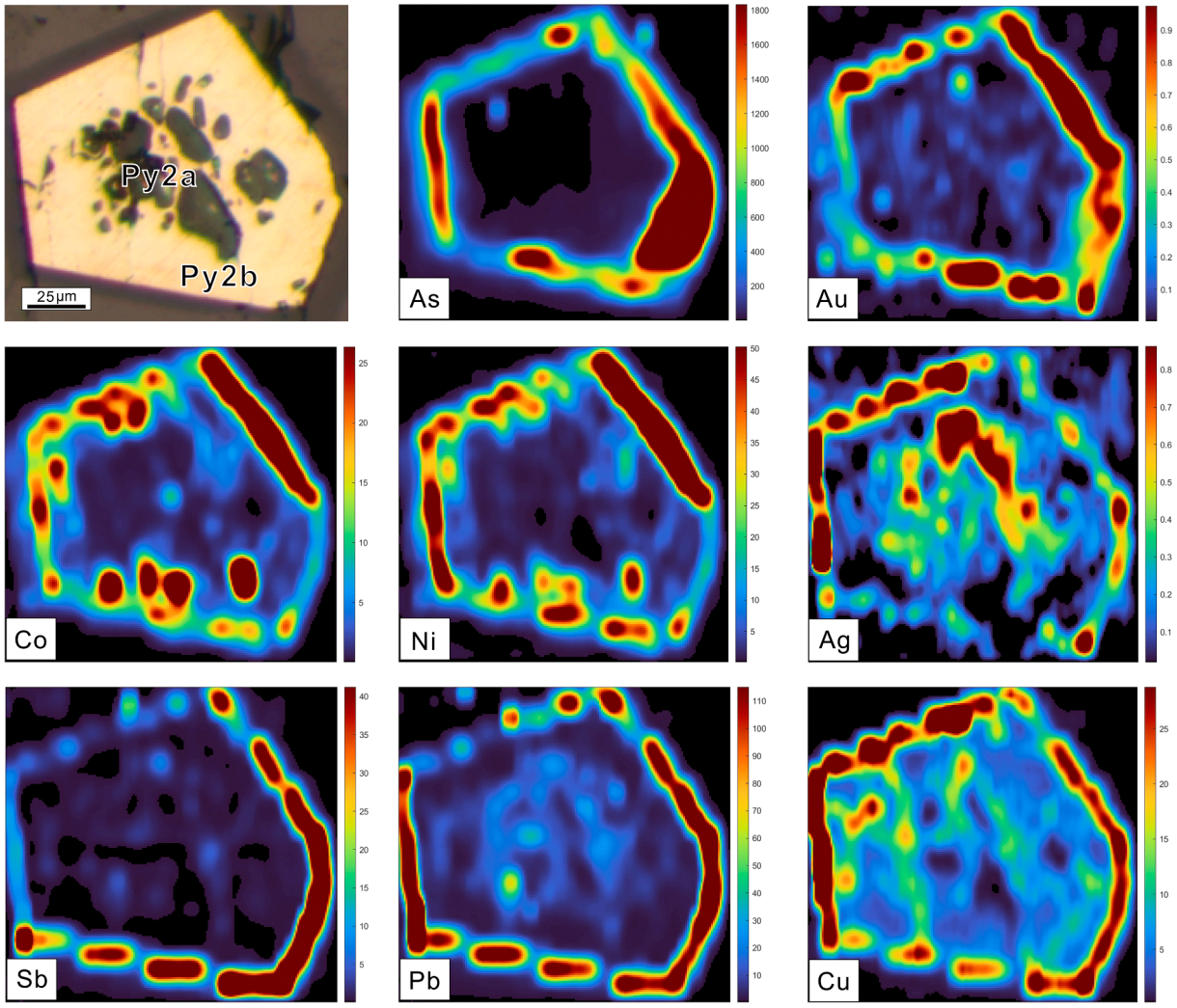

Fig. 9. LA–ICP–MS multielement mapping of selected pyrite from the Pianyanzi gold deposit.

Zn, Pb, Bi, Se, Ti, Sb, and Ge concentrations. The contents of some trace elements such as Mo, Sn, Tl, Te and rare earth element (REE) are typically below the detection limit.

Py1 is relatively enriched in As and Se, with averages of 3348.21 ppm and 24.56 ppm, respectively. As shown in Fig. 10, Py1 is commonly depleted in Au, Ag, Co, Ni, Sb, Pb and Bi with average concentrations of 0.68 ppm, 0.06 ppm, 0.28 ppm, 1.77 ppm, 3.94 ppm, 6.05 ppm and 0.8 ppm, respectively.

Py2a has the highest concentrations of Mg (average 1154.69 ppm) and Ca (average 2400.69 ppm); relatively high concentrations of Cu (average 45.22 ppm), Co (average 8.64 ppm), Ni (average 9.18 ppm), Se (48.74), Sb (average 15.63 ppm), Pb (average 118.57 ppm), and Bi (average 3.76 ppm); and the lowest concentrations of As (average 185.82 ppm) and Au (average 0.75 ppm). Compared with Py2a, Py2b shows significantly higher As and Au contents ranging from 616.68 to 10656.39 ppm and 0.27 to 12.48 ppm, respectively. Additionally, Py2b shows slightly increasing Co and Ni concentrations and decreasing Cu, Sb and Bi concentrations. Some elements, such as Ag and Se, have similar concentrations. By LA–ICP–MS mapping of the selected zoned pyrite grains (Py2a & Py2b), we obtained clear elemental distribution patterns of Co, Ni, Cu, As, Ag, Sb, Au and Pb. As shown in the LA–ICP–MS trace element maps (Figs. 8–9), there is noticeable chemical zoning from the porous and inclusion-rich core (Py2a) to the rim (Py2b), which is coherent with EPMA mapping. The overgrowth (Py2b) has higher concentrations of elements such as As, Au, Co, Ni and Cu compared to Py1a.

Py3 exhibits relatively high concentrations of Pb and Sb, averaging 98.49 ppm and 12.68 ppm, respectively. Conversely, Py3 has lower Ag, with a mean of 0.73 ppm, and Bi is below the detection line, with Co, Ni, Cu and Zn similar to Py1. In addition, the As content is lower compared to Py1 (mean 1929.48 ppm). For Py4, the Co and Ni concentrations are comparable to those of Py3. However, it has higher Ag (average 43.38 ppm) and Se (average 43.38 ppm) levels, and lower Pb (average 0.14 ppm) and Bi (average 0.12 ppm) concentrations than other types of pyrite.

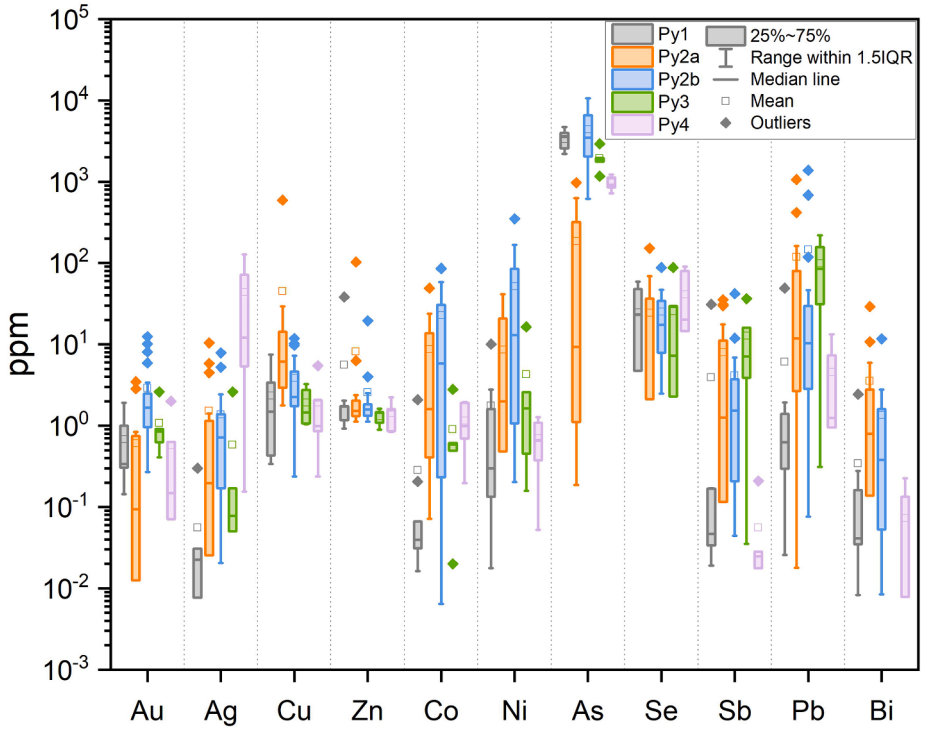

Fig. 10. Box and whisker diagram showing selective trace element contents of the different pyrites from Pianyanzi.

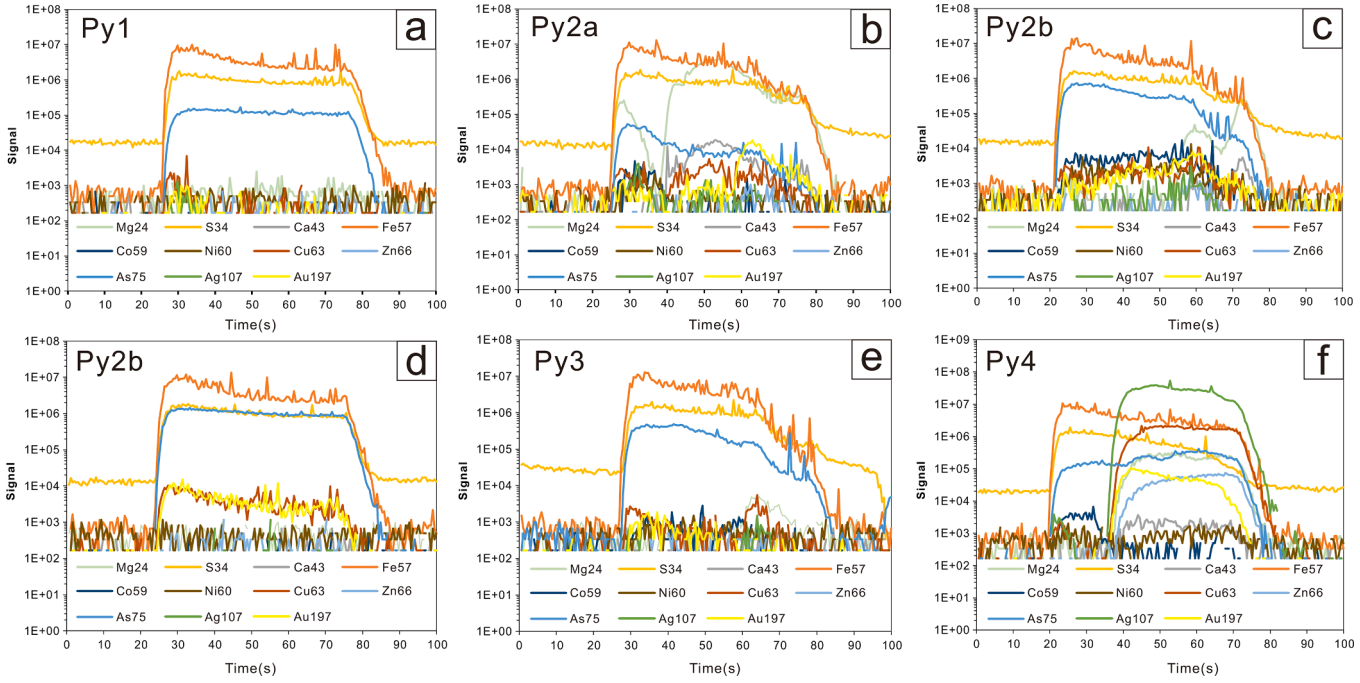

Fig. 11. Representative LA–ICP–MS time-resolved spectra for each pyrite generation from Pianyanzi, showing the distribution of Mg, S, Ca, Fe, Co, Ni, Cu, Zn, As, Ag and Au.

4.4. In-situ sulfur isotopic compositions of pyrite

The *in-situ* S isotopic compositions of the different types of pyrite are given in Table 3. The pyrite from the Pianyanzi Au deposit typically exhibits positive $\delta^{34}S$ values ranging between 1.49 and 7.08 ‰, except for one spot from Py2a, which shows a negative $\delta^{34}S$ value of −0.52 ‰. Py1 displays a limited range of $\delta^{34}S$ values, ranging from 6.50 to 6.85 ‰ (mean = 6.63 ‰), whereas Py3 and Py4 have comparable $\delta^{34}S$ values ranging from 5.95 to 7.08 ‰ with an average of 6.5 ‰. In comparison, the $\delta^{34}S$ value of Py2a is low, ranging from −0.52 to 3.25 ‰, while that of Py2b is between 6.44 and 6.97 ‰, which is consistent with the $\delta^{34}S$ values of Py1, Py3 and Py4.

Table 3
Sulfur isotope compositions of different pyrite types from Pianyanzi.

Sample	Pyrite types	$\delta^{34}S_{V\text{-}CDT}$ (‰)	Delta-2SE
56-04-3-t-1-1	Py1	6.50	0.08
56-06-1-t-3-1	Py1	6.83	0.11
56-06-1-t-2-1	Py1	6.97	0.07
56-08-1-t-2-1	Py1	6.57	0.08
56-01-et-1-1	Py2a	2.40	0.17
56-02-2-t-4-1	Py2a	3.25	0.10
56-06-1-t-1-1	Py2a	2.80	0.07
56-12-Bt-1-1	Py2a	1.49	0.09
56-12-Bt-1-2	Py2a	−0.52	0.09
56-01-et-1-2	Py2b	6.68	0.12
56-02-2-t-1-1	Py2b	6.44	0.09
56-02-2-t-3-1	Py2b	6.58	0.07
56-02-2-t-4-2	Py2b	6.64	0.13
56-12-Bt-1-3	Py2b	6.52	0.11
P2-11-B-J-4-1	Py2b	6.49	0.08
56-5-T-5-1-1	Py3	5.95	0.09
56-5-T-5-2-1	Py3	6.45	0.10
P2-08-A-J-2-1	Py4	7.08	0.07

5. Discussion

5.1. Pyrite information and gold occurrence

Textural and chemical variations among different pyrite generations (Py1, Py2a, Py2b, Py3 and Py4) were observed by means of EMPA and LA–ICP–MS analyses in spot and mapping modes. In addition, the time-resolved ablation profiles of individual laser spot analyses can be used to identify invisible or nano-sized inclusions within pyrite grains (Maslennikov et al., 2009; Genna and Gaboury, 2015). However, if the nano-inclusions are evenly distributed, it may appear impossible to detect them by LA–ICP–MS depth profiles (Cook et al., 2016). In that case, co-variations between specific elements can provide us useful clues for their identification (Voute et al., 2019).

Our petrographic observations have demonstrated that native gold particles are widely distributed throughout the gold-forming stages (Fig. 5d–i). This visible native Au delineates a significant Au species at Pianyanzi. Our *in-situ* analyses also revealed the distribution characteristics of gold in pyrite. Specifically, the average concentrations of Au in different pyrite generations are 0.68 (0.14–1.90 ppm) in Py1, 0.75 ppm (bdl–3.47 ppm) in Py2a, 2.99 ppm (0.27–12.48 ppm) in Py2b, 1.08 ppm (0.41–2.61 ppm) in Py3, and 0.71 ppm (bdl–2.00 ppm) in Py4. The compositional points on Au and As all appear below the solubility lines defined by Reich et al. (2005) in an Au–As scatterplot (Fig. 12a), indicating that Au^{+} is a dominant form in the crystal lattice of pyrite. More evidence for the occurrence of gold in the lattice sites comes from the flat time-resolved ablation profiles of gold in most pyrite grains (Fig. 11). Considering the low concentrations of Au (<2 ppm in average) in pyrite and other mineral inclusions or nanoparticles (e.g., sulfide) potentially encapsulated therein, gold in the form of Au^{+} is not a dominant form in the ores of the Pianyanzi deposit.

The positive correlation between Au and Cu (Fig. 12b) together with the smooth laser ablation spectra suggest that Au^{3+} and Cu^{+} ions replaced two Fe^{2+} ions in a coupled substitution process (Chouinard et al., 2005), that required anomalous oxidation conditions (Hazarika et al., 2013). Such substitutions could happen during the late stage because there are abundant oxide minerals such as hematite formed during Stage 4. The concentrations of Ag and Sb in pyrite demonstrate no positive correlations with Au (Fig. 12c and Fig. 12e), indicating a decoupling of Au and Ag and/or a lack of electrum inclusions (Voute et al., 2019). Due to significant differences in ionic size, it is challenging for Pb to get incorporated into the lattice of pyrite (Chinnasamy et al., 2021). Accordingly, the positive correlations between Pb and Ag and between Pb and Bi (Fig. 12d and Fig. 12f), are likely due to the presence of galena inclusions (Shao et al., 2018). The occurrence of various sulfide nanoparticles in pyrite is typical of hydrothermal deposits (e.g.,

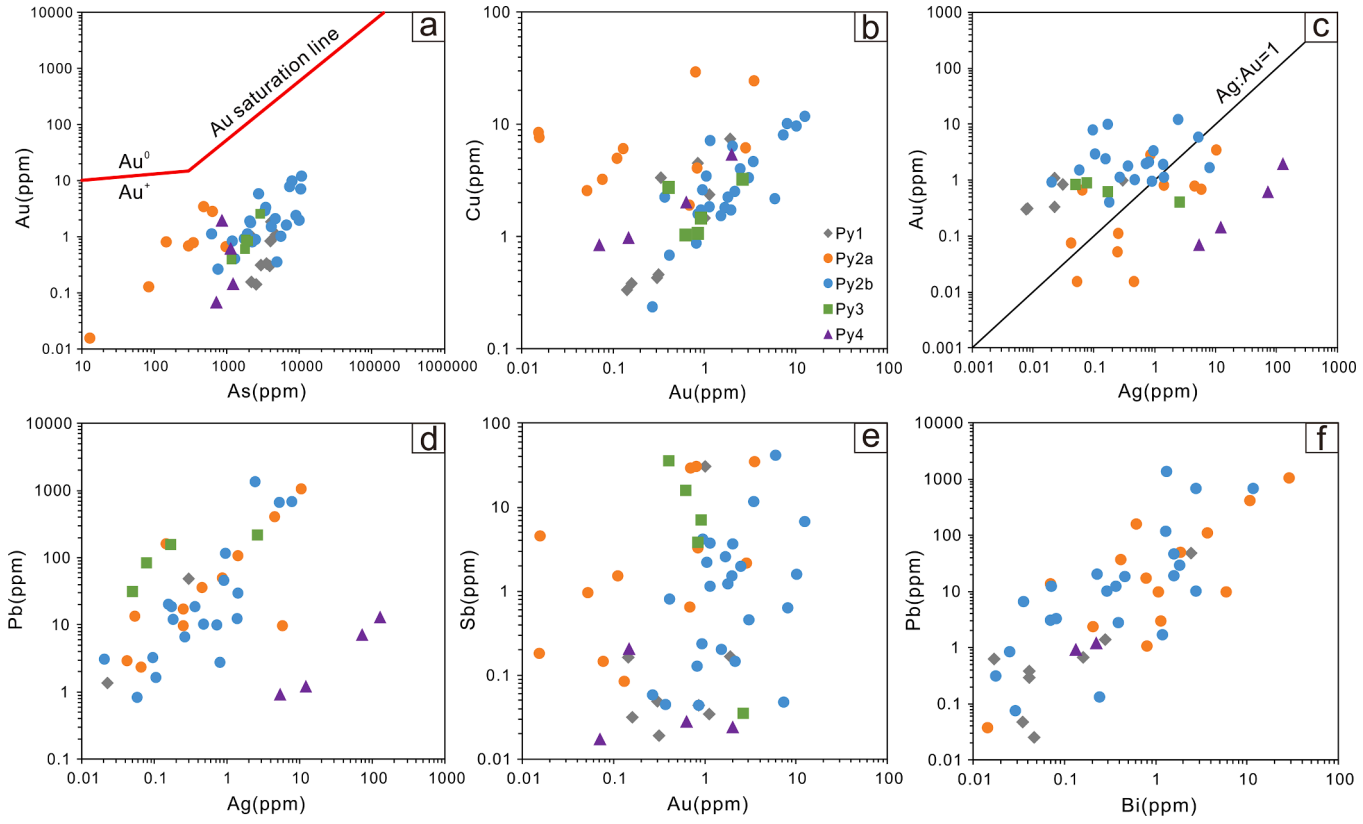

Fig. 12. Binary plots of As vs. Au (the Au saturation line is defined by Reich et al. 2005), Cu vs. Au, Au vs. Ag, Pb vs. Ag, Sb vs. Au, and Pb vs. Bi from each pyrite generation from Pianyanzi.

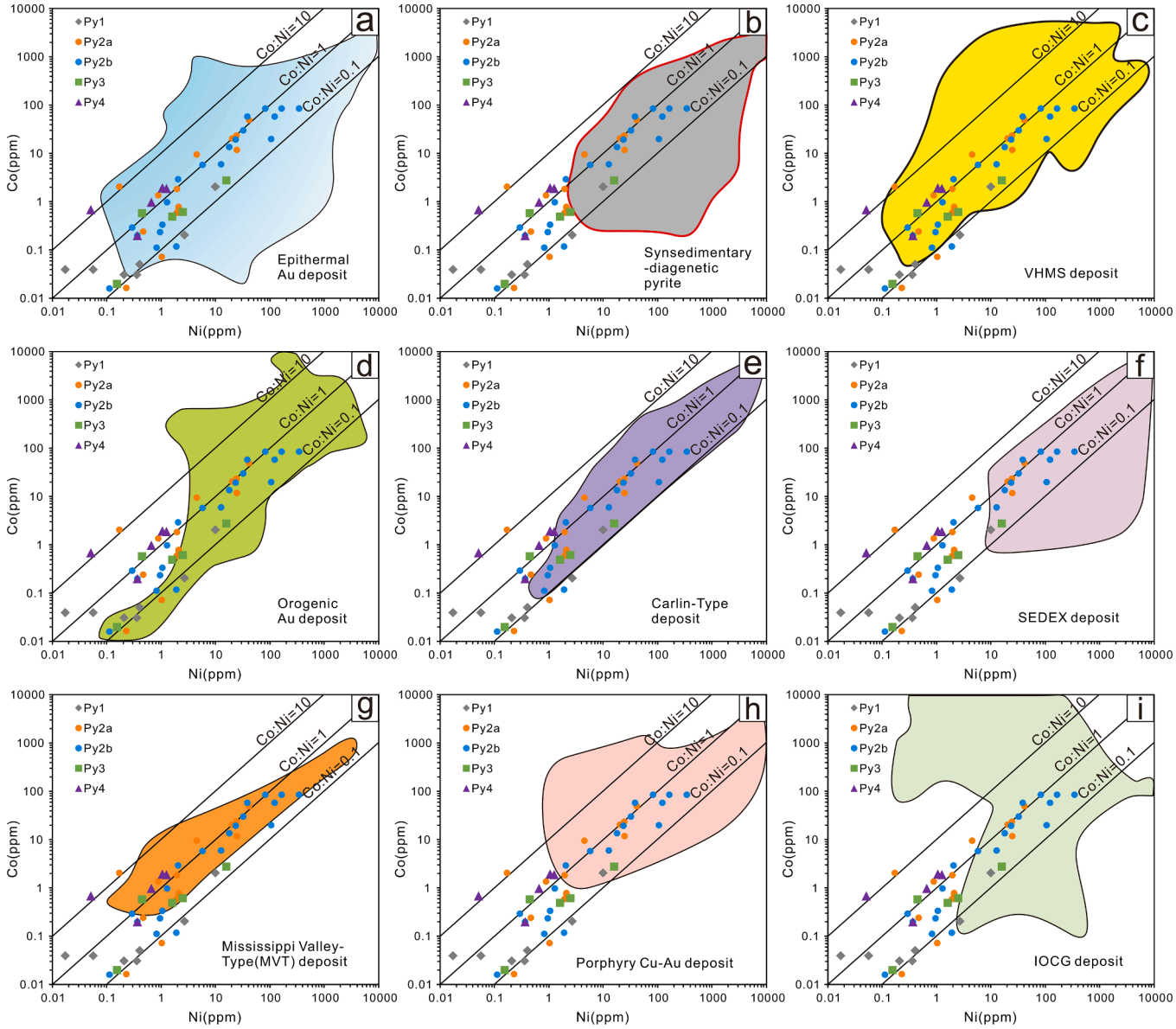

Fig. 13. Correlation between Co and Ni concentrations and Co/Ni ratios of pyrites from other typical deposits (modified after Baidya et al. 2021).

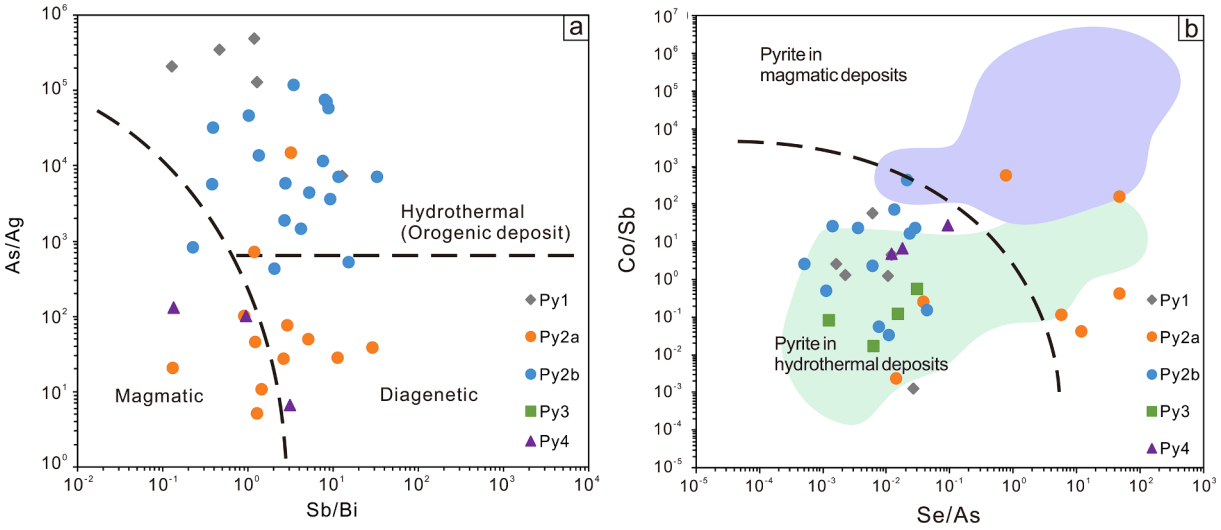

Fig. 14. Binary diagrams of the (a) As/Ag–Sb/Bi and (b) Co/Sb–Se/As of the pyrites from Pianyanzi (modified after Augustin and Gaboury, 2019; Duran et al. 2019).

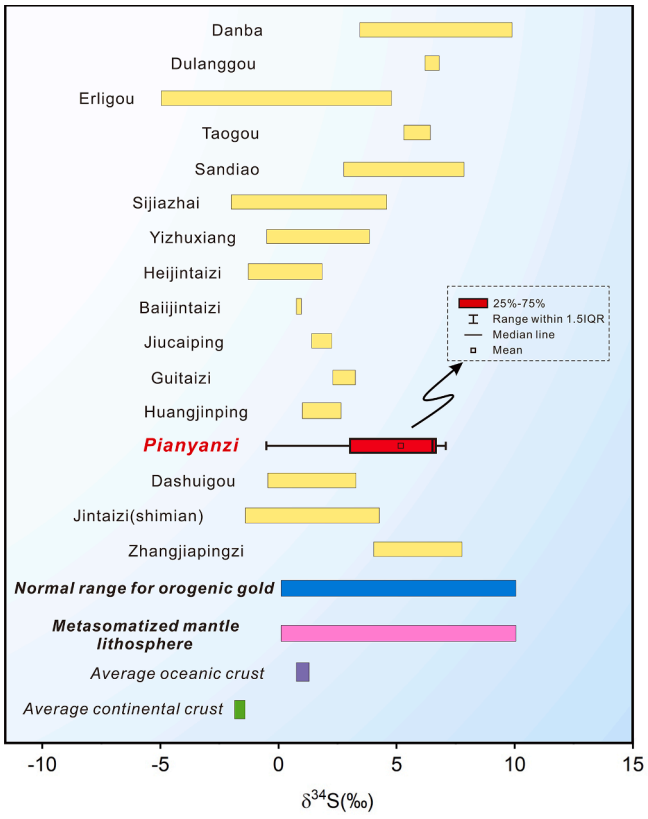

Fig. 15. Diagram showing the $\delta^{34}S$ values of pyrites from Pianyanzi. Comparable data include orogenic gold deposits on the western margin of the Yangtze Craton (see Supplementary Table 4 for details), normal range for orogenic gold deposits (Goldfarb and Groves, 2015), metasomatized mantle lithosphere (Wang et al., 2020) and average continental and oceanic crust (Rielli et al., 2018).

Deditius et al., 2011; Chinnasamy et al., 2021). In our case, this is supported by the following evidences: 1) galena particles can be observed within the pyrite grains in the BSE images (Fig. 7c and Fig. 7e), and 2) there are occasional peaks with relevant element signals in the time-resolved laser ablation profiles (Fig. 11b and Fig. 11e).

Arsenic typically occurs in its As^{1-} anionic state involved in the partial replacement of S within the crystal lattice of pyrite (Savage et al., 2000; Deditius et al., 2014). The emplacement of As into the pyrite lattice can enhance its ability to host Au in hydrothermal systems (Large et al., 2007; Gopon et al., 2019; Kusebauch et al., 2019; Pokrovski et al., 2021). The bivariate plot (Fig. 12a) displays a broad positive correlation between Au and As, which is consistent with the preferential precipitation of Au. The concentrations of As in Py1, Py2a, Py2b, Py3 and Py4 are 3348.21 ppm, 185.82 ppm, 4460.23 ppm, 1929.48 ppm and 967.71 ppm, respectively. The concentrations of As in Stage 2 pyrites (from Py2a to Py2b) are much more variable compared to Py1, Py3 and Py4. The Py2a&b preserved distinctive chemical zonation. LA–ICP–MS mapping demonstrates a systematic increase in the trace elements (e.g., Au, As, Co, Ni, Ag, Sb, Pb and Cu) from Py2a to Py2b (Figs. 8–9). The formation of zoned pyrite grains in Pianyanzi reflects rapid variations in fluid compositions (Deditius et al., 2014), that could be ascribed to fluid-rock interactions or fluid boiling (Velásquez et al., 2014; Li et al., 2018; Berthier et al., 2023; Lin et al., 2023; Xing et al., 2023). Note, compared to other pyrite types, Py2a typically shows more porous and inclusion-rich textures compared to other types of pyrite (Fig. 5d–g and Fig. 7c–d). An alternative explanation could be a coupled dissolution-reprecipitation (CDR) reaction (Velásquez et al., 2014; Chinnasamy et al., 2021; Ma et al., 2022; Tan et al., 2022), suggesting that Py2b is a product of the CDR reaction of Py2a with subsequent infiltrated fluids.

Co/Ni ratios have been used by many researchers to help elucidate the origin of pyrite (e.g., Bajwah et al., 1987; Large et al., 2009; Reich et al., 2016). Specifically, pyrite of sedimentary origin is characterized by low Co/Ni ratios (<1), while pyrite of hydrothermal origin exhibits higher Co/Ni ratios (>1). The concentrations of Co and Ni in pyrite are positively correlated (Fig. 13). Figure 13a–i demonstrates a large overlap in the Co/Ni ratio data from various deposit types (Baidya et al., 2021). This overlap makes differentiating the types of deposits based on the trace element scatter plots only difficult. However, the elemental distribution plots could help to constrain the range of deposit types (Gregory et al., 2019). The Co/Ni ratios for Py1 range from 0.01 to 2.24 (0.51 in average). For Py2a and Py2b, the Co/Ni ratios range from 0.07 to 11.86 and 0.04 to 1.48 (1.58 and 0.57 in average), respectively. For Py3, the Co/Ni ratios range from 0.13 to 13.2 with an average of 2.06. Our results are consistent with the model for the formation of orogenic gold deposits by Belousov et al. (2016), which implies that 65 % of "orogenic" pyrites have Co/Ni ratios < 1, and 94 % have Co/Ni ratios < 10. The As/Ag vs. Sb/Bi and Co/Sb vs. Se/As diagrams (Fig. 14a–b) support rather a hydrothermal than magmatic origin of most pyrites under study (Augustin and Gaboury, 2019; Duran et al., 2019).

5.2. Source of sulfur

Our petrographic investigations show the absence of sulfate minerals in the Pianyanzi gold deposit, suggesting that H_2S may act as the dominant sulfur species (Ohmoto, 1972). Therefore, the measured $\delta^{34}S$ values of pyrite can serve as the sulfur isotope of the ore fluid (Hiroshi and Ohmoto, 1986; Cao et al., 2019).

The $\delta^{34}S$ values obtained from the Pianyanzi deposit range from −0.52 ‰ to 7.08 ‰ and form two groups. The first group, Py2a, displays the $\delta^{34}S$ values ranging from −0.52 ‰ to 3.25 ‰, with an average value of 1.88 ‰. The other generations of pyrite are homogeneous and yield higher $\delta^{34}S$ values spanning 5.95 ‰ to 7.08 ‰. Multiple fluid processes, such as fluid mixing, wall rock interactions, and isotopic fractionation, have a potential to modify the $\delta^{34}S$ ratios of mineral fluids (see discussion in Sun et al. 2020). Note, the variations of $\delta^{34}S$ are typically observed in pyrite grains with zoning, ranging from Py2a (core) to Py2b (rim), where there was an increase in $\delta^{34}S$ values (Fig. 7c–d). Notably, trace elements also show coupled variation characteristics from Py2a to Py2b, which may be caused by fluid-rock interactions, fluid boiling and/or CDR reactions (Oberthuer et al., 1996; Uemoto et al., 2002; Hodkiewicz et al., 2009; Goldfarb and Groves, 2015; Yang et al., 2023). With the exception of slightly lower $\delta^{34}S$ values in Py2a, the sulfur isotope compositions of pyrite at Pianyanzi are homogeneous, indicative of a homogeneous fluid source.

There are typical ranges of $\delta^{34}S$ values from different sources: magmatic sulfur (−3‰ to 7 ‰; Hiroshi and Ohmoto, 1986); granitoid (1.0 ± 6.1 ‰; Robert, 2006), sedimentary sulfur (<0, Rollinson, 1994), primitive mantle (0 ± 3 ‰; Ohomoto and Rye, 1979) and marine sulfur (20 ‰; Rollinson, 1994). The $\delta^{34}S$ values obtained from Pianyanzi exhibit similarity to those reported in metasomatized mantle lithosphere (Fig. 15), as documented by Zhao et al. (2019), Wang et al. (2020) and Zhao et al. (2022b). Additionally, the $\delta^{34}S$ variations at Pianyanzi are consistent with those of the hypozonal, mesozonal and epizonal gold deposits of the Daduhe gold belt (~0 to 10 ‰; Zhao et al., 2022a). The aforementioned evidence suggests that the gold deposits, including Pianyanzi, within the Daduhe gold belt could have a relatively consistent ore-fluid source, which is mainly derived from the deep metasomatized mantle lithosphere.

5.3. Mechanisms of gold precipitation

Although both visible Au and invisible Au (Au^+) occurred, the dominant form of gold present in Pianyanzi is native gold grains. The precipitation of native gold may be due to the CDR reactions of previously auriferous pyrite (Fougerouse et al., 2016; Hastie et al., 2020) or direct precipitation from ore fluids (Taylor et al., 2021). Considering the very low gold content in the pyrite under study, direct native gold deposition was the major ore-forming process. The prevalence of native gold in pyrites or along their grain boundaries (Fig. 5e–g) suggests that the ore-forming fluid was enriched in reduced sulfur and that the gold was transported predominantly as an Au–HS complex (Stefánsson and Seward, 2004; Williams-Jones et al., 2009).

Petrographic observations indicate that gold is primarily enriched during Stage 2, which is distinguished by the extensive generation of sellaite. In addition, previous research (e.g. Li, 1997) has demonstrated that there is a high abundance of CO_2 phases in fluid inclusions of the Pianyanzi gold deposit. Based on geological exploration and experimental data, we provisionally propose the following scenario of mineralization. An auriferous fluid ascended along regional faults triggered by compressional tectonics at the western margin of the Yangtze Craton. Then the gold as an Au–HS complex was transported to favorable sites (e.g., the NNE fault). During the ascent, a range of fluid processes including fluid-rock interactions ensued, resulting in the extraction of substances (e.g., Mg^{2+}, Ca^{2+}). A series of potential reactions (Eqs. 1–3) probably produced the native gold and an associated sellaite-bearing mineral assemblage.

$$2Au(HS)_2^- + 2F^- + Mg^{2+} + CO_2 + H_2O = 2Au\downarrow + MgF_2\downarrow + S\downarrow + 3H_2S\uparrow + 2HCO_3^- \quad (1)$$

$$2Au(HS)_2^- + 2F^- + Ca^{2+} + CO_2 + H_2O = 2Au\downarrow + CaF_2\downarrow + S\downarrow + 3H_2S\uparrow + 2HCO_3^- \quad (2)$$

$$2Au(HS)_2^- + Fe^{2+} = Au\downarrow + FeS_2\downarrow + 2H_2S\uparrow \quad (3)$$

Based on the laser ablation spectra (Fig. 11c), Mg and Ca were detected as inclusions in Py2b. In addition to sellaite and fluorite, natural sulphur (S) was identified in hand specimens (Fig. 3d), supporting the plausibility of the above reactions. Stage 4 is another stage of native gold mineralization, which is characterized by abundant hematite intergrown with pyrite (Fig. 5h–i). Such a phenomenon was also reported for the Naakenavaara orogenic gold deposits of the Central Lapland belt, northern Finland (Vasilopoulos et al., 2023). The precipitation of gold during this stage could be linked to rapid changes of the physico-chemical conditions of the hydrothermal system (Evans, 2010).

6. Conclusions

We studied the Pianyanzi sellaite-bearing orogenic gold deposit located in the western margin of the Yangtze Craton using a novel combination of petrographic investigations, EMPA, LA–ICP–MS trace element analysis, multielement mapping and *in-situ* sulfur isotopes. We identified five stages of deposit establishment: pre-ore stage, three stages of mineralization, sellaite-bearing gold, galena-dominated sulfide, and hematite-bearing gold, and post-ore oxidation.

We identified five generations of pyrite, Py1, Py2a, Py2b, Py3, and Py4, possessing distinctive textural and geochemical characteristics. The Pianyanzi deposit is dominated by native gold, but the new LA–ICP–MS data indicate the presence of trace invisible gold as Au^+ in the crystal lattice of pyrite. Our petrographic observations show that the deposition of gold peaked during the second ore stage, which corresponds to the formation of Py2a&b. The LA–ICP–MS spot analyses and mapping indicate a systematic increase in the concentrations of trace elements such as Au, As, Co, Ni, Ag, Sb, Pb, and Cu from Py2a to Py2b, suggesting that fluid-rock interactions, fluid boiling and/or CDR reactions may have occurred. The $\delta^{34}S$ values (−0.52 ‰ to 7.08 ‰) observed in Pianyanzi, coupled with the consistently recorded $\delta^{34}S$ values (~0 to 10 ‰) from other orogenic deposits of the Daduhe gold belt, indicate a relatively consistent ore-fluid source that originated from metasomatized mantle lithosphere.

A series of potential reactions of the interaction between auriferous fluids and wall rocks (e.g., dolomite) were probably responsible for the deposition of native gold and associated sellaite-bearing mineral assemblage.

Declaration of competing interest

The authors declare that they have no known competing financial interests or personal relationships that could have appeared to influence the work reported in this paper.

Data availability

Data will be made available on request.

Acknowledgments

This work was funded by the National Natural Science Foundation of China (42302104), the Sichuan Natural Science Foundation (2022NSFSC0410) and the Fundamental Research Funds for the Central Universities of China (2682023CX016). We thank Dr. Yun-Hui Zhang for helping with the field work. Xi Chen, Yong Yin and Hao Wu are also thanked for the help with lab work. We would like to thank the editor-in-chief Prof. Huayong Chen and two anonymous reviewers for their comments, which helped us considerably to improve this paper.

Appendix A. Supplementary data

Supplementary data to this article can be found online at https://doi.org/10.1016/j.oregeorev.2023.105866.

References

Augustin, J., Gaboury, D., 2019. Multi-stage and multi-sourced fluid and gold in the formation of orogenic gold deposits in the world-class Mana district of Burkina Faso – Revealed by LA-ICP-MS analysis of pyrites and arsenopyrites. Ore Geol. Rev. 104, 495–521.

Baidya, A.S., Sen, A., Pal, D.C., Upadhyay, D., 2021. Ore-forming processes in the Khetri Copper Belt, western India: constraints from trace element chemistry of pyrite and C-O isotope composition of carbonates. Miner. Deposita 56, 957–974.

Bajwah, Z.U., Seccombe, P.K., Offler, R., 1987. Trace element distribution Co: Ni ratios and genesis of the Big Cadia iron-copper deposit, New South Wales, Australia. Mineral. Deposita. 22, 292–300.

Barley, M.E., Groves, D.I., 1992. Supercontinent cycles and the distribution of metal deposits through time. Geology 20, 291–294.

Belousov, I., Large, R.R., Meffre, S., Danyushevsky, L.V., Steadman, J., Beardsmore, T., 2016. Pyrite compositions from VHMS and orogenic Au deposits in the Yilgarn Craton, Western Australia: Implications for gold and copper exploration. Ore Geol. Rev. 79, 474–499.

Berthier, C., Perret, J., Eglinger, A., André-Mayer, A.S., Feneyrol, J., Voinot, A., Teitler, Y., Bosc, R., 2023. Pyrite as a microtextural and geochemical tracer of ore-forming processes, central zone orogenic gold deposit, Gabgaba District. Sudan. Economic Geology. 118, 1031–1053.

Bierlein, F.P., Groves, D.I., Cawood, P.A., 2009. Metallogeny of accretionary orogens — The connection between lithospheric processes and metal endowment. Ore Geol. Rev. 36, 282–292.

Broom-Fendley, S., Brady, A.E., Wall, F., Gunn, G., Dawes, W., 2017. REE minerals at the Songwe Hill carbonatite, Malawi: HREE-enrichment in late-stage apatite. Ore Geol. Rev. 81, 23–41.

Cao, H.-W., Zou, H., Bagas, L., Zhang, L.-K., Zhang, Z., Li, Z.-Q., 2019. The Laqiong Sb-Au deposit: Implications for polymetallic mineral systems in the Tethys-Himalayan zone of southern Tibet. China. Gondwana Research. 72, 83–96.

Cao, H.-W., Li, G.-M., Zhang, R.-Q., Zhang, Y.-H., Zhang, L.-K., Dai, Z.-W., Zhang, Z., Liang, W., Dong, S.-L., Xia, X.-B., 2021. Genesis of the Cuonadong tin polymetallic deposit in the Tethyan Himalaya: Evidence from geology, geochronology, fluid inclusions and multiple isotopes. Gondw. Res. 92, 72–101.

Cao, H.W., Pei, Q.M., Zhang, S.T., Zhang, L.K., Tang, L., Lin, J.Z., Zheng, L., 2017. Geology, geochemistry and genesis of the Eocene Lailishan Sn deposit in the Sanjiang region, SW China. J. Asian Earth Sci. 137, 220–240.

Cao, H.-W., Pei, Q.-M., Santosh, M., Li, G.-M., Zhang, L.-K., Zhang, X.-F., Zhang, Y.-H., Zou, H., Dai, Z.-W., Lin, B., Tang, L., Yu, X., 2022. Himalayan leucogranites: A review of geochemical and isotopic characteristics, timing of formation, genesis, and rare metal mineralization. Earth Sci. Rev. 234, 104229.

Cao, H.-W., Pei, Q.-M., Yu, X., Cao, A.-B., Chen, Y., Liu, H., Zhang, K., Liu, X., Zhang, X.-F., 2023a. The long-lived partial melting of the Greater Himalayas in southern Tibet, constraints from the geochronology and geochemistry of the Miocene Gyirong anatectic pegmatite. China Geology. 6, 303–321.

Cao, H.-W., Pei, Q.-M., Yu, X., Santosh, M., Li, G.-M., Zhang, L.-K., Zou, H., Dong, L., Gao, K., Dai, Z.-W., Ai, J.-B., Lan, S.-S., Xiang, F., Cao, A.-B., 2023b. Discovery of the large-scale Eocene Xiwu Pb–Zn–Ag deposit in the Tethyan Himalaya: Geochronology, geochemistry, and C-H–O–S–Pb–Sr–Nd isotopes. Gondw. Res. 124, 165–187.

Chao, W., Ye, H., Tang, X., Zhang, Z., Wang, H., 2023. Textural, trace element, and sulfur isotope analyses of pyrite from the Yindongpo deposit, East Qinling Orogen: Implications for gold mineralization. Ore Geol. Rev. 105796.

Chinnasamy, S.S., Uken, R., Reinhardt, J., Selby, D., Johnson, S., 2015. Pressure, temperature, and timing of mineralization of the sedimentary rock-hosted orogenic gold deposit at Klipwal, southeastern Kaapvaal Craton. South Africa. Mineralium Deposita. 50, 739–766.

Chinnasamy, S.S., Hazarika, P., Pal, D., Sen, R., Govindaraj, G., 2021. Pyrite textures and trace element compositions from the granodiorite-hosted gold deposit at jonnagiri, eastern dharwar craton, india: Implications for gold mineralization processes. Econ. Geol. 116, 559–579.

Chouinard, A., Paquette, J., Williams-Jones, A.E., 2005. Crystallographic controls on trace-element incorporation in Auriferous pyrite from the Pascua epithermal high-sulfidation deposit. Chile-Argentina. Canadian Mineralogist. 43, 951–963.

Cook, N.J., Ciobanu, C.L., Mao, J., 2009. Textural control on gold distribution in As-free pyrite from the Dongping, Huangtuliang and Hougou gold deposits, North China Craton (Hebei Province, China). Chem. Geol. 264, 101–121.

Cook, N., Ciobanu, C., George, L., Zhu, Z.-Y., Wade, B., Ehrig, K., 2016. Trace Element Analysis of Minerals in Magmatic-Hydrothermal Ores by Laser Ablation Inductively-Coupled Plasma Mass Spectrometry: Approaches and Opportunities. Minerals. 6, 111.

Craig, J.R., Vokes, F.M., Solberg, T.N., 1998. Pyrite: physical and chemical textures. Miner. Deposita 34, 82–101.

Deditius, A.P., Utsunomiya, S., Reich, M., Kesler, S.E., Ewing, R.C., Hough, R., Walshe, J., 2011. Trace metal nanoparticles in pyrite. Ore Geol. Rev. 42, 32–46.

Deditius, A.P., Reich, M., Kesler, S.E., Utsunomiya, S., Chryssoulis, S.L., Walshe, J., Ewing, R.C., 2014. The coupled geochemistry of Au and As in pyrite from hydrothermal ore deposits. Geochim. Cosmochim. Acta 140, 644–670.

Deng, J., Wang, Q., 2016. Gold mineralization in China: Metallogenic provinces, deposit types and tectonic framework. Gondw. Res. 36, 219–274.

Deng, J., Wang, Q., Li, G., Li, C., Wang, C., 2014. Tethys tectonic evolution and its bearing on the distribution of important mineral deposits in the Sanjiang region, SW China. Gondwana Res. 26, 419–437.

Duran, C.J., Dubé-Loubert, H., Pagé, P., Barnes, S.-J., Roy, M., Savard, D., Cave, B.J., Arguin, J.-P., Mansur, E.T., 2019. Applications of trace element chemistry of pyrite and chalcopyrite in glacial sediments to mineral exploration targeting: Example from the Churchill Province, northern Quebec, Canada. J. Geochem. Explorat. 196, 105–130.

Evans, K.A., 2010. A test of the viability of fluid–wall rock interaction mechanisms for changes in opaque phase assemblage in metasedimentary rocks in the Kambalda-St. Ives goldfield, Western Australia. Miner. Deposita 45, 207–213.

Fontboté, L., Kouzmanov, K., Chiaradia, M., Pokrovski, G.S., 2017. Sulfide Minerals in Hydrothermal Deposits. Elements 13, 97–103.

Fougerouse, D., Micklethwaite, S., Tomkins, A.G., Mei, Y., Kilburn, M., Guagliardo, P., Fisher, L.A., Halfpenny, A., Gee, M., Paterson, D., Howard, D.L., 2016. Gold remobilisation and formation of high grade ore shoots driven by dissolution-reprecipitation replacement and Ni substitution into auriferous arsenopyrite. Geochim. Cosmochim. Acta 178, 143–159.

Fu, J., Hu, Z., Zhang, W., Yang, L., Liu, Y., Li, M., Zong, K., Gao, S., Hu, S., 2016. In situ sulfur isotopes (δ34S and δ33S) analyses in sulfides and elemental sulfur using high sensitivity cones combined with the addition of nitrogen by laser ablation MC-ICP-MS. Anal. Chim. Acta 911, 14–26.

Gebre-Mariam, M., Hagemann, S.G., Groves, D.I., 1995. A classification scheme for epigenetic Archaean lode-gold deposits. Miner. Deposita 30, 408–410.

Genna, D., Gaboury, D., 2015. Deciphering the Hydrothermal Evolution of a VMS System by LA-ICP-MS Using Trace Elements in Pyrite: An Example from the Bracemac-McLeod Deposits, Abitibi, Canada, and Implications for Exploration. Econ. Geol. 110, 2087–2108.

Goldfarb, R.J., Baker, T., Dubé, B., Groves, D.I., Hart, C.J.R., Gosselin, P., Hedenquist, J. W., Thompson, J.F.H., Goldfarb, R.J., Richards, J.P., 2005. Distribution, character, and genesis of gold deposits in metamorphic terran. Econ. Geol. 100th Anniversary Volume, 407–450.

Goldfarb, R.J., Groves, D.I., 2015. Orogenic gold: Common or evolving fluid and metal sources through time. Lithos 233, 2–26.

Goldfarb, R.J., Groves, D.I., Gardoll, S., 2001. Orogenic gold and geologic time: a global synthesis. Ore Geol. Rev. 18, 1–75.

Goldfarb, R.J., Pitcairn, I., 2023. Orogenic gold: is a genetic association with magmatism realistic? Miner. Deposita 58, 5–35.

Goldfarb, R., Qiu, K., Deng, J., Chen, Y., Yang, L., 2019. Orogenic Gold Deposits of China. In: Chang, Z., Goldfarb, R.J. (Eds.), Mineral Deposits of. Society of Economic Geologists, China, pp. 263–324.

Gopon, P., Douglas, J.O., Auger, M.A., Hansen, L., Wade, J., Cline, J.S., Robb, L.J., Moody, M.P., 2019. A nanoscale investigation of carlin-type gold deposits: an atom-scale elemental and isotopic perspective. Econ. Geol. 114, 1123–1133.

Gregory, D.D., Large, R.R., Bath, A.B., Steadman, J.A., Wu, S., Danyushevsky, L., Bull, S. W., Holden, P., Ireland, T.R., 2016. trace element content of pyrite from the Kapai Slate, St. Ives Gold District, Western Australia. Econ. Geol. 111, 1297–1320.

Gregory, D.D., Cracknell, M.J., Large, R.R., McGoldrick, P., Kuhn, S., Maslennikov, V.V., Baker, M.J., Fox, N., Belousov, I., Figueroa, M.C., Steadman, J.A., Fabris, A.J., Lyons, T.W., 2019. Distinguishing ore deposit type and barren sedimentary pyrite using laser ablation-inductively coupled plasma-mass spectrometry trace element data and statistical analysis of large data sets. Econ. Geol. 114, 771–786.

Groves, D.I., Goldfarb, R.J., Gebre-Mariam, M., Hagemann, S.G., Robert, F., 1998. Orogenic gold deposits: A proposed classification in the context of their crustal distribution and relationship to other gold deposit types. Ore Geol. Rev. 13, 7–27.

Groves, D.I., Santosh, M., 2021. Craton and thick lithosphere margins: The sites of giant mineral deposits and mineral provinces. Gondw. Res. 100, 195–222.

Groves, D.I., Santosh, M., Goldfarb, R.J., Zhang, L., 2018. Structural geometry of orogenic gold deposits: Implications for exploration of world-class and giant deposits. Geosci. Front. 9, 1163–1177.

Groves, D.I., Santosh, M., Deng, J., Wang, Q., Yang, L., Zhang, L., 2020. A holistic model for the origin of orogenic gold deposits and its implications for exploration. Miner. Deposita 55, 275–292.

Hastie, E.C.G., Kontak, D.J., Lafrance, B., 2020. Gold Remobilization: Insights from Gold Deposits in the Archean Swayze Greenstone Belt, Abitibi Subprovince, Canada. Econ. Geol. 115, 241–277.
Hazarika, P., Mishra, B., Saravanan Chinnasamy, S., Bernhardt, H.-J., 2013. Multi-stage growth and invisible gold distribution in pyrite from the Kundarkocha sediment-hosted gold deposit, eastern India. Ore Geol. Rev. 55, 134–145.
Hiroshi, O., 1986. Stable isotope geochemistry of ore deposits. Rev. Mineral. Geochem. 16, 491–559.
Hodkiewicz, P.F., Groves, D.I., Davidson, G.J., Weinberg, R.F., Hagemann, S.G., 2009. Influence of structural setting on sulphur isotopes in Archean orogenic gold deposits, Eastern Goldfields Province, Yilgarn, Western Australia. Mineral. Deposita. 44, 129–150.
Hu, X.-K., Tang, L., Zhang, S.-T., Santosh, M., Spencer, C.J., Zhao, Y., Cao, H.-W., Pei, Q.-M., 2019. In situ trace element and sulfur isotope of pyrite constrain ore genesis in the Shapoling molybdenum deposit, East Qinling Orogen, China. Ore Geol. Rev. 105, 123–136.
Hu, Z., Zhang, W., Liu, Y., Gao, S., Li, M., Zong, K., Chen, H., Hu, S., 2015. "Wave" signal-smoothing and mercury-removing device for laser ablation quadrupole and multiple collector ICPMS analysis: application to lead isotope analysis. Anal. Chem. 87, 1152–1157.
Huston, D.L., Blewett, R.S., Champion, D.C., 2012. Australia through time: a summary of its tectonic and metallogenic evolution. Episodes 35, 23–43.
Kapp, P., DeCelles, P.G., 2019. Mesozoic-Cenozoic geological evolution of the Himalayan-Tibetan orogen and working tectonic hypotheses. Am. J. Sci. 319, 159–254.
Keith, M., Smith, D.J., Doyle, K., Holwell, D.A., Jenkin, G.R.T., Barry, T.L., Becker, J., Rampe, J., 2020. Pyrite chemistry: A new window into Au-Te ore-forming processes in alkaline epithermal districts, Cripple Creek, Colorado. Geochim. Cosmochim. Acta. 274, 172–191.
Koenig, A.E., Rogers, R.R., Trueman, C.N., 2009. Visualizing fossilization using laser ablation–inductively coupled plasma–mass spectrometry maps of trace elements in Late Cretaceous bones. Geology 37, 511–514.
Koglin, N., Frimmel, H.E., Minter, W.E.L., Brätz, H., 2010. Trace-element characteristics of different pyrite types in Mesoarchaean to Palaeoproterozoic placer deposits. Miner. Deposita 45, 259–280.
Kusebauch, C., Gleeson, S.A., Oelze, M., 2019. Coupled partitioning of Au and As into pyrite controls formation of giant Au deposits. Science. Advances 5, eaav5891.
Large, R.R., Maslennikov, V.V., Fo, R., Danyushevsky, L.V., Chang, Z., 2007. Multistage Sedimentary and Metamorphic Origin of Pyrite and Gold in the Giant Sukhoi Log Deposit, Lena Gold Province, Russia. Econ. Geol. 102, 1233–1267.
Large, R.R., Danyushevsky, L., Hollit, C., Maslennikov, V., Meffre, S., Gilbert, S., Bull, S., Scott, R., Emsbo, P., Thomas, H., Singh, B., Foster, J., 2009. Gold and trace element zonation in pyrite using a laser imaging technique: Implications for the timing of gold in orogenic and carlin-style sediment-hosted deposits. Econ. Geol. 104, 635–668.
Large, R.R., Bull, S.W., Maslennikov, V.V., 2011. A Carbonaceous Sedimentary Source-Rock Model for Carlin-Type and Orogenic Gold Deposits. Econ. Geol. 106, 331–358.
Li B. 1997. A research for fluid inclusions from Pianyanzi gold deposit, Kangding. Acta Geologica Sichuan. 17, 36-42 (in Chinese with English abstract).
Li, B., Cai, J., 1995. Physicochemical conditions of mineralization and the transportation and deposition of Au in Pianyanzi gold deposit. Journal of Chengdu Institute of Technology. 22, 89–95 (in Chinese with English abstract).
Li, X.-H., Fan, H.-R., Yang, K.-F., Hollings, P., Liu, X., Hu, F.-F., Cai, Y.-C., 2018. Pyrite textures and compositions from the Zhuangzi Au deposit, southeastern North China Craton: implication for ore-forming processes. Contrib. Miner. Petrol. 173, 73.
Li, X., Mao, J., Wang, C., Watanabe, Y., 2007. The Daduhe gold field at the eastern margin of the Tibetan Plateau: He, Ar, S, O, and H isotopic data and their metallogenic implications. Ore Geol. Rev. 30, 244–256.
Li, H., Zhang, Z., Santosh, M., Lü, L., Han, L., Liu, W., Cheng, Z., 2016. Late Permian basalts in the northwestern margin of the Emeishan Large Igneous Province: Implications for the origin of the Songpan-Ganzi terrane. Lithos 256–257, 75–87.
Lin, S., Hu, K., Cao, J., Liu, Y., Liu, S., Zhang, B., 2023. Coupling and decoupling of Au and As in pyrite from Carlin-type Au deposits, southwest China. J. Asian Earth Sci. 246, 105582.
Liu, Y., Hu, Z., Gao, S., Günther, D., Xu, J., Gao, C., Chen, H., 2008. In situ analysis of major and trace elements of anhydrous minerals by LA-ICP-MS without applying an internal standard. Chem. Geol. 257, 34–43.
Lu, Y., Mao, Y., 1988. Analysis of the characteristics of ore-controlling structures in Kangding Pianyanzi gold ore deposit. J. Chengdu Coll. Geol. 15, 11–19 (in Chinese with English abstract).
Luo, H., Mao, Y., Lu, Y., Shi, A., Fan, S., Cai, J., Yu, S., 1987. The geology of Pianyanzi sellaite type gold ore deposit, Kangding County, Sichuan Province. Sichuan Publishing House of Science Technology, Chengdu (in Chinese with English abstract).
Ma, Y., Jiang, S., Frimmel, H.E., Zhu, L., 2022. In situ chemical and isotopic analyses and element mapping of multiple-generation pyrite: Evidence of episodic gold mobilization and deposition for the Qiucun epithermal gold deposit in Southeast China. Am. Mineral. 107, 1133–1148.
Mao, Y., Lu, Y., Cai, J., Shuai, D., 1986. A new type of gold deposit-Kangding Pianyanzi fluoromagnesite type gold deposit. Journal of Chengdu College of. Geology, 6–9 (in Chinese with English abstract.
Martin, A.J., Jamieson, J.W., de Ronde, C.E.J., Layne, G.D., Piercey, G., Brandl, P.A., 2023. Constraining temporal variations in metal and sulfur sources using high-resolution mineral-scale analysis of pyrite: evidence from the Brothers volcano, Kermadec arc, New Zealand. Mineralium Deposita. 58, 1237–1262.
Maslennikov, V.V., Maslennikova, S.P., Large, R.R., Danyushevsky, L.V., 2009. Study of Trace Element Zonation in Vent Chimneys from the Silurian Yaman-Kasy Volcanic-Hosted Massive Sulfide Deposit (Southern Urals, Russia) Using Laser Ablation-Inductively Coupled Plasma Mass Spectrometry (LA-ICPMS). Econ. Geol. 104, 1111–1141.
Metcalfe, I., 2021. Multiple Tethyan ocean basins and orogenic belts in Asia. Gondw. Res. 100, 87–130.
Oberthuer, T., Mumm, A.S., Vetter, U., Simon, K., Amanor, J.A., 1996. Gold mineralization in the Ashanti Belt of Ghana: genetic constraints of the stable isotope geochemistry. Econ. Geol. 91, 289–301.
Ohmoto, H., 1972. Systematics of Sulfur and Carbon Isotopes in Hydrothermal Ore Deposits. Econ. Geol. 67, 551–578.
Ohomoto, H., Rye, R.O., 1979. Isotopes of sulfur and carbon. Geochem. Hydrothermal Ore Deposits.
Pei, Q.-M., Li, C.-H., Zhang, S.-T., Zou, H., Liang, Y., Wang, L., Li, S.-L., Cao, H.-W., 2022. Vein-type fluorite mineralization of the Linxi district in the Great Xing'an Range, Northeast China: Insights from geochronology, mineral geochemistry, fluid inclusion and stable isotope systematics. Ore Geol. Rev. 142, 104708.
Pei, Q., Zhang, S., Santosh, M., Cao, H., Zhang, W., Hu, X., Wang, L., 2017. Geochronology, geochemistry, fluid inclusion and C, O and Hf isotope compositions of the Shuitou fluorite deposit, Inner Mongolia, China. Ore Geol. Rev. 83, 174–190.
Phillips, G.N., Powell, R., 2009. Formation of gold deposits: Review and evaluation of the continuum model. Earth Sci. Rev. 94, 1–21.
Pokrovski, G.S., Escoda, C., Blanchard, M., Testemale, D., Hazemann, J.L., Gouy, S., Kokh, M.A., Boiron, M.C., de Parseval, F., Aigouy, T., Menjot, L., de Parseval, P., Proux, O., Rovezzi, M., Béziat, D., Salvi, S., Kouzmanov, K., Bartsch, T., Pöttgen, R., Doert, T., 2021. An arsenic-driven pump for invisible gold in hydrothermal systems. Geochem. Perspect. Lett. 17, 39–44.
Qiu, K.-F., Yu, H.-C., Deng, J., McIntire, D., Gou, Z.-Y., Geng, J.-Z., Chang, Z.-S., Zhu, R., Li, K.-N., Goldfarb, R., 2020. The giant Zaozigou Au-Sb deposit in West Qinling, China: magmatic- or metamorphic-hydrothermal origin? Miner. Deposita 55, 345–362.
Raič, S., Molnár, F., O'Brien, H., Cook, N., Vasilopoulos, M., 2023. Building geochemical vectors with trace element compositions of sulfides in orogenic gold mineral systems in northern Finland. J. Geochem. Explor. 251, 107252.
Reich, M., Kesler, S.E., Utsunomiya, S., Palenik, C.S., Chryssoulis, S.L., Ewing, R.C., 2005. Solubility of gold in arsenian pyrite. Geochim. Cosmochim. Acta 69, 2781–2796.
Reich, M., Simon, A.C., Deditius, A., Barra, F., Chryssoulis, S., Lagas, G., Tardani, D., Knipping, J., Bilenker, L., Sanchez-Alfaro, P., Roberts, M.P., Munizaga, R., 2016. Trace element signature of pyrite from the los colorados iron oxide-apatite (IOA) Deposit, Chile: A missing link between andean ioa and iron oxide copper-gold systems? Econ. Geol. 111, 743–761.
Rielli, A., Tomkins, A.G., Nebel, O., Raveggi, M., Jeon, H., Martin, L., Ávila, J.N., 2018. Sulfur isotope and PGE systematics of metasomatised mantle wedge. Earth Planet. Sci. Lett. 497, 181–192.
Robert, F., Brommecker, R., Bourne, B., Dobak, P.J., McEwan, C., Rowe, R.R., Zhou, X., 2007. Models and exploration methods for major gold deposit types. In: Proceedings of Exploration 07: Fifth Decennial International Conference on Mineral Exploration, pp. 691–711.
Roger, F., Jolivet, M., Malavieille, J., 2010. The tectonic evolution of the Songpan-Garzê (North Tibet) and adjacent areas from Proterozoic to Present: A synthesis. J. Asian Earth Sci. 39, 254–269.
Rollinson, H.R., 1994. Using Geochemical Data. Mineral. Mag. 58, 523.
Safonova, I., Perfilova, A., 2023. Survived and disappeared intra-oceanic arcs of the Paleo-Asian Ocean: evidence from Kazakhstan. Natl. Sci. Rev. 10, nwac215.
Savage, K.S., Tingle, T.N., O'Day, P.A., Waychunas, G.A., Bird, D.K., 2000. Arsenic speciation in pyrite and secondary weathering phases, Mother Lode Gold District, Tuolumne County, California. Appl. Geochem. 15, 1219–1244.
Shao, Y.-J., Wang, W.-S., Liu, Q.-Q., Zhang, Y., 2018. Trace element analysis of pyrite from the zhengchong gold deposit, Northeast Hunan Province, China: implications for the ore-forming process. Minerals. 8, 262.
Stefánsson, A., Seward, T.M., 2004. Gold(I) complexing in aqueous sulphide solutions to 500°C at 500 bar. Geochim. Cosmochim. Acta 68, 4121–4143.
Su, T., Spicer, R.A., Li, S.H., Xu, H., Huang, J., Sherlock, S., Huang, Y.J., Li, S.F., Wang, L., Jia, L.B., Deng, W.Y., Liu, J., Deng, C.L., Zhang, S.T., Valdes, P.J., Zhou, Z. K., 2019. Uplift, climate and biotic changes at the Eocene-Oligocene transition in south-eastern Tibet. Natl. Sci. Rev. 6, 495–504.
Sun, P., Wang, Q., Li, H., Dong, C., Deng, J., 2020. Geology and pyrite sulfur isotopes of the Suoluogou gold deposit: Implication for crustal continuum model of orogenic gold deposit in northwestern margin of Yangtze Craton. SW China. Ore Geology Reviews. 122, 103487.
Tan, W., Reddy, S.M., Fougerouse, D., Wang, C.Y., Wei, B., Xian, H., Yang, Y., He, H., 2022. Superimposed microstructures of pyrite in auriferous quartz veins as fingerprints of episodic fluid infiltration in the Wulong Lode gold deposit, NE China. Mineralium Deposita. 57, 685–700.
Tanner, D., Henley, R.W., Mavrogenes, J.A., Holden, P., 2016. Sulfur isotope and trace element systematics of zoned pyrite crystals from the El Indio Au–Cu–Ag deposit, Chile. Contribut. Mineral. Petrol. 171, 33.
Taylor, R.D., Monecke, T., Reynolds, T.J., Monecke, J., 2021. Paragenesis of an orogenic gold deposit: new insights on mineralizing processes at the Grass Valley District, California. Econ. Geol. 116, 323–356.
Uemoto, T., Ridley, J., Mikucki, E., Groves, D.I., Kusakabe, M., 2002. Fluid chemical evolution as a factor in controlling the distribution of Gold at the Archean Golden Crown Lode Gold Deposit, Murchison Province, Western Australia. Econ. Geol. 97, 1227–1248.

Velásquez, G., Béziat, D., Salvi, S., Siebenaller, L., Borisova, A.Y., Pokrovski, G.S., De Parseval, P., 2014. Formation and Deformation of Pyrite and Implications for Gold Mineralization in the El Callao District, Venezuela. Econ. Geol. 109, 457–486.
Voute, F., Hagemann, S.G., Evans, N.J., Villanes, C., 2019. Sulfur isotopes, trace element, and textural analyses of pyrite, arsenopyrite and base metal sulfides associated with gold mineralization in the Pataz-Parcoy district, Peru: implication for paragenesis, fluid source, and gold deposition mechanisms. Miner. Deposita 54, 1077–1100.
Wallis, S., Tsujimori, T., Aoya, M., Kawakami, T., Terada, K., Suzuki, K., Hyodo, H., 2003. Cenozoic and Mesozoic metamorphism in the Longmenshan orogen: Implications for geodynamic models of eastern Tibet. Geology 31, 745–748.
Wang, D., Mao, J., Yan, S., Yang, J., Xu, J., Chen, Y., Xue, C., 2005. Episodes of Cenozoic Gold Mineralization on the Eastern Margin of the Qinghai-Tibet Plateau: $^{40}Ar/^{39}Ar$ Dating and Implication for Geodynamic Events. Acta Geol. Sinica-Engl. Ed. 79, 233–253.
Wang, H., Xia, Q., Zhou, Z., Lei, L., Chen, C., Yang, P., Gong, Y., Hua, Q., Bao, Q., 2023. Orogenic gold mineralization in the Huangling region and its intimate tectonic linkage to the Neoproterozoic orogeny of South China. Precambr. Res. 394, 107105.
Wang, Q., Zhao, H., Groves, D.I., Deng, J., Zhang, Q., Xue, S., 2020. The Jurassic Danba hypozonal orogenic gold deposit, western China: indirect derivation from fertile mantle lithosphere metasomatized during Neoproterozoic subduction. Miner. Deposita 55, 309–324.
Wang, Q., Yang, L., Zhao, H., Groves, D.I., Weng, W., Xue, S., Li, H., Dong, C., Yang, L., Li, D., Deng, J., 2022. Towards a universal model for orogenic gold systems: A perspective based on Chinese examples with geodynamic, temporal, and deposit-scale structural and geochemical diversity. Earth Sci. Rev. 224, 103861.
Weatherley, D.K., Henley, R.W., 2013. Flash vaporization during earthquakes evidenced by gold deposits. Nat. Geosci. 6, 294–298.
Williams-Jones, A.E., Bowell, R.J., Migdisov, A.A., 2009. Gold in solution. Elements 5, 281–287.
Wu, Y.-F., Li, J.-W., Evans, K., Koenig, A.E., Li, Z.-K., O'Brien, H., Lahaye, Y., Rempel, K., Hu, S.-Y., Zhang, Z.-P., Yu, J.-P., 2018. Ore-Forming Processes of the Daqiao Epizonal Orogenic Gold Deposit, West Qinling Orogen, China: Constraints from Textures, Trace Elements, and Sulfur Isotopes of Pyrite and Marcasite, and Raman Spectroscopy of Carbonaceous Material. Econ. Geol. 113, 1093–1132.
Vasilopoulos, M., Molnár, F., Ranta, J.-P., O'Brien, H., 2023. Mineralogical, lithogeochemical and sulfide trace element characteristics of the Hirvilavanmaa Au-only and the base metal-rich Naakenavaara orogenic gold deposits in the Central Lapland belt, northern Finland. J. Geochem. Explor. 244, 107132.
Xing, L., Li, W., Yang, F., Zhao, X., Symons, D.T.A., Seltmann, R., Liu, B., 2023. Contribution of carbonaceous strata to intrusion–related Au mineralization: Evidence from trace elements and S-Pb isotopes in pyrite from the Qukulekedong Au–Sb deposit, East Kunlun. NW China. Gondwana Research. 122, 23–40.
Xu, J.-F., Suzuki, K., Xu, Y.-G., Mei, H.-J., Li, J., 2007. Os, Pb, and Nd isotope geochemistry of the Permian Emeishan continental flood basalts: Insights into the source of a large igneous province. Geochim. Cosmochim. Acta 71, 2104–2119.
Yan, D.P., Zhou, M.F., Li, S.B., Wei, G.Q., 2011. Structural and geochronological constraints on the Mesozoic-Cenozoic tectonic evolution of the Longmen Shan thrust belt, eastern Tibetan Plateau. Tectonics 30, TC6005.
Yan, D.-P., Zhou, Y., Qiu, L., Wells, M.L., Mu, H., Xu, C.-G., 2018. The Longmenshan Tectonic Complex and adjacent tectonic units in the eastern margin of the Tibetan Plateau: A review. J. Asian Earth Sci. 164, 33–57.
Yang, L.-Q., Deng, J., Groves, D.I., Santosh, M., He, W.-Y., Li, N., Zhang, L., Zhang, R.-R., Zhang, H.-R., 2022. Metallogenic 'factories' and resultant highly anomalous mineral endowment on the craton margins of China. Geosci. Front. 13, 101339.
Yang, L., Wang, Q., Large, R.R., Mukherjee, I., Deng, J., Li, H., Yu, H., Wang, X., 2021. Fluid source and metal precipitation mechanism of sediment-hosted Chang'an orogenic gold deposit, SW China: Constraints from sulfide texture, trace element, S, Pb, and He-Ar isotopes and calcite C-O isotopes. Am. Mineral. 106, 410–429.
Yang, L., Wang, Q., Groves, D.I., Li, H., Zhai, D., Wang, X., Deng, J., 2023. Mineral assemblages, fluid inclusions, pyrite trace elements, and s-o isotopes of gold ores from the cenozoic daping deposit, SW China: Implications for the genesis of complex orogenic lode gold systems. Econ. Geol. 118, 903–926.
Zeng, Y., Wang, Q., Groves, D.I., Santosh, M., Wang, Y., Wang, T., Yang, L., Chen, W., Deng, J., 2023. Prolonged Mesozoic intracontinental gold mineralization in the South China Block controlled by lithosphere architecture and evolving Paleo-Pacific Plate subduction. Earth Sci. Rev. 240, 104387.
Zhang, W., Hu, Z., Liu, Y., 2020. Iso-Compass: new freeware software for isotopic data reduction of LA-MC-ICP-MS. J. Anal. At. Spectrom 35, 1087–1096.
Zhang, Y., Li, Y., Yi, X., Chen, C., Wang, J., Yang, Y., Zhou, F., 2022. Geological characteristics and occurrence status of gold in the Pianyanzi gold deposit in the Dadu River Basin, Sichuan Province. Multipurpose Utilization of Mineral Resource 42–47 (in Chinese with English abstract).
Zhang, Z., Mao, J., Saunders, A.D., Ai, Y., Li, Y., Zhao, L., 2009. Petrogenetic modeling of three mafic–ultramafic layered intrusions in the Emeishan large igneous province, SW China, based on isotopic and bulk chemical constraints. Lithos 113, 369–392.
Zhang, Y., Yan, D.-P., Qiu, L., Gong, L., Shao, Y., 2023. Stepwise growth of the southeastern Tibetan Plateau: Structural and thermochronological evidence from the Panxi tectonic belt. Palaeogeogr. Palaeoclimatol. Palaeoecol. 621, 111542.
Zhao, H., Wang, Q., Groves, D.I., Deng, J., 2019. A rare Phanerozoic amphibolite-hosted gold deposit at Danba, Yangtze Craton, China: significance to fluid and metal sources for orogenic gold systems. Miner. Deposita 54, 133–152.
Zhao, H., Wang, Q., Groves, D.I., Deng, J., 2021. Progressive spatial and temporal evolution of tectonic triggers and metasomatized mantle lithosphere sources for orogenic gold mineralization in a Triassic convergent margin: Kunlun-Qinling Orogen, central China. GSA Bull. 133, 2378–2392.
Zhao, H., Wang, Q., Groves, D.I., Santosh, M., Zhang, J., Fan, T., 2022a. Genesis of orogenic gold systems in the Daduhe belt: Evidence of long-lived fertile mantle lithosphere as a source of diverse metallogeny on the western margin of the Yangtze Craton, China. Ore Geol. Rev. 145, 104861.
Zhao, H., Wang, Q., Kendrick, M.A., Groves, D.I., Fan, T., Deng, J., 2022b. Metasomatized mantle lithosphere and altered ocean crust as a fluid source for orogenic gold deposits. Geochim. Cosmochim. Acta 334, 316–337.
Zhao, J.-H., Zhou, M.-F., 2008. Neoproterozoic adakitic plutons in the northern margin of the Yangtze Block, China: Partial melting of a thickened lower crust and implications for secular crustal evolution. Lithos 104, 231–248.
Zheng, D., 1995. Exploration of Several Migration Forms of Gold and Discussion on the Metallogenic Mechanism of Kangding Pianyanzi Fluoromagnesite Gold Deposit. Acta Geol. Sichuan. 15, 304–311 in Chinese with English abstract.
Zhou, Z., Chen, Z., Weyer, S., Horn, I., Huo, H., Zhang, W., Li, N., Zhang, Q., Han, F., Feng, H., 2023. Metal source and ore precipitation mechanism of the Ashawayi orogenic gold deposit, southwestern Tianshan Orogen, western China: Constraints from textures and trace elements in pyrite. Ore Geol. Rev. 157, 105452.
Zhou, M., Ma, Y., Yan, D., Xia, X., Zhao, J., Sun, M., 2006. The Yanbian Terrane (Southern Sichuan Province, SW China): A Neoproterozoic arc assemblage in the western margin of the Yangtze Block. Precambr. Res. 144, 19–38.
Zhou, M.-F., Yan, D.-P., Kennedy, A.K., Li, Y., Ding, J., 2002. SHRIMP U-Pb zircon geochronological and geochemical evidence for Neoproterozoic arc-magmatism along the western margin of the Yangtze Block, South China. Earth Planet. Sci. Lett. 196, 51–67.
Zou, H., Li, Q.-L., Bagas, L., Wang, X.-C., Chen, A.-Q., Li, X.-H., 2021. A Neoproterozoic low-$\delta^{18}O$ magmatic ring around South China: Implications for configuration and breakup of Rodinia supercontinent. Earth Planet. Sci. Lett. 575, 117196.